

Uncertainty Quantification of Surrogate Models using Conformal Prediction

Vignesh Gopakumar*

*UCL Centre for Artificial Intelligence
Department of Computer Science
University College London
London, WC1V 6LJ, UK*

V.GOPAKUMAR@UCL.AC.UK

Ander Gray*

*Heudiasyc Laboratory
Université de Technologie de Compiègne
Compiègne, 60200, France*

ANDER.GRAY@HDS.UTC.FR

Joel Oskarsson

*Department of Computer and Information Science
Linköping University
Linköping, 581 83, Sweden*

JOEL.OSKARSSON@LIU.SE

Lorenzo Zanisi

*Computing Division
UK Atomic Energy Authority
Oxford, OX14 3EB, UK*

LORENZO.ZANISI@UKAEA.UK

Stanislas Pamela

*Computing Division
UK Atomic Energy Authority
Oxford, OX14 3EB, UK*

STANISLAS.PAMELA@UKAEA.UK

Daniel Giles

*UCL Centre for Artificial Intelligence
Department of Computer Science
University College London
London, WC1V 6LJ, UK*

D.GILES@UCL.AC.UK

Matt J. Kusner

*UCL Centre for Artificial Intelligence
Department of Computer Science
University College London
London, WC1V 6LJ, UK*

M.KUSNER@UCL.AC.UK

Marc Peter Deisenroth

*UCL Centre for Artificial Intelligence
Department of Computer Science
University College London
London, WC1V 6LJ, UK*

M.DEISENROTH@UCL.AC.UK

*. These authors contributed equally to this work

Abstract

Data-driven surrogate models have shown immense potential as quick, inexpensive approximations to complex numerical and experimental modelling tasks. However, most surrogate models of physical systems do not quantify their uncertainty, rendering their predictions unreliable, requiring further validation. Though Bayesian approximations offer some solace in estimating the error associated with these models, they cannot provide guarantees, and the quality of their inferences depends on the availability of prior information and good approximations to posteriors for complex problems. This is particularly pertinent to multi-variable or spatio-temporal problems. Our work constructs and formalises a conformal prediction framework that satisfies marginal coverage for spatio-temporal predictions in a model-agnostic manner, requiring near-zero computational costs. We provide an extensive empirical study of the application of the framework to ascertain valid error bars that provide guaranteed coverage across the surrogate model's domain of operation. The application scope of our work extends across a large range of spatio-temporal models, from solving partial differential equations to weather forecasting. Through the applications, the paper looks at providing statistically valid error bars for deterministic models, as well as crafting guarantees to the error bars of probabilistic models. Our conformal prediction formalisation provides guaranteed coverage of the surrogate model, regardless of model architecture, and its training regime and is unbothered by the curse of dimensionality.

Keywords: Surrogate Models, Uncertainty Quantification, Conformal Prediction, Neural-PDE, Neural-Weather

1 Introduction

Partial Differential Equations (PDEs) governing physical processes are solved using complex numerical modelling simulation codes. Though these codes offer a mathematically-rigorous method of solving the relevant equations, the solutions are often limited to discretised domains and require computationally-expensive iterative solvers like finite-volume schemes and finite-element methods. Such simulation codes have become central to multiple scientific disciplines in biology (Hospital, Adam et al., 2015), engineering (Giudicelli et al., 2024), and climate science (Danabasoglu et al., 2020) (Lavin et al., 2021), but they are difficult to deploy for rapid, iterative modelling, which is often required while exploring a design space of solutions. Machine learning offers an alternative data-driven route for obtaining quick, inexpensive approximations to numerical simulations (Bertone et al., 2019; Karniadakis et al., 2021). Data-driven surrogate models are often built by distilling the spatio-temporal information characterised by the simulations into parameterised machine learning models. Due to the efficiency, cost-effectiveness, and relative accuracy of modelling, neural networks have become ubiquitous within scientific modelling, and they are of primary importance in tackling large-scale PDEs in climate (Lam et al., 2023; Kurth et al., 2023), computational fluid dynamics (Jiang et al., 2020; Pfaff et al., 2021), and nuclear fusion (van de Plassche et al., 2020; Gopakumar and Samaddar, 2020).

As effective as these surrogate models (emulators) are, they remain approximations of the true physical system under study. There are often many layers of approximations as the simulation codes approximate the PDEs and the PDEs themselves are approximations to the true physical system. They often fail to quantify the uncertainty associated with their approximation, i.e. the approximation error of the emulator with that of the numerical code. Irrespective of the domain of operation they were trained on, models often claim confident

outputs. This is problematic for two reasons: (a) without an assessment of the confidence of the output, erroneous predictions can lead to severe consequences downstream; (b) The cost of training these models can be prohibitively high, and without appropriate uncertainty quantification the overconfident predictions have limited utility in practice. Several works have attempted to provide uncertainty estimation for these surrogate models (Geneva and Zabaras, 2020; Alhajeri et al., 2022; Zou et al., 2024; Psaros et al., 2023), but they fail to provide statistical guarantees over the error bars attached to the prediction and to scale to complex scenarios (Abdar et al., 2021). They also require ensemble training Lakshminarayanan et al. (2017), extensive sampling (MacKay, 1992), or architectural modifications (Gal and Ghahramani, 2016), successively increasing the amount of computational resources required. There remains a concerning question of validating the surrogate model’s outputs for a specific downstream application.

Conformal prediction (CP) (Vovk et al., 2005) provides a framework that allows us to compute statistically guaranteed error bars over pre-trained and fine-tuned models, i.e. the error bars are calibrated to provide the required coverage. Conformal prediction relies on the calibration of model performance across a specific dataset representative of the desired prediction distribution, and utilising the calibration measures to help provide valid error bars for the model output.

In this paper, we conduct a thorough empirical study on conformal prediction for neural-network-based surrogate models to equip their predictions with calibrated, guaranteed error bars, even on out-of-training-distribution scenarios. We demonstrate guaranteed coverage across spatio-temporal domains (high-dimensional outputs), irrespective of the choice of model, data and training conditions. Our work provides a rigorous method to check the *usefulness* of a pre-trained surrogate model, its validity and applicability in an inference/production scenario.

We conduct an empirical study that demonstrates at scale the estimation of statistically guaranteed error bars for pre-trained and fine-tuned surrogate models using conformal prediction. Our focus lies on extending the conformal prediction framework to work for models predicting over a spatio-temporal domain. Through experimentation of increasing complexity, we demonstrate how we can provide guaranteed error bars for various kinds of neural-network-based surrogate models. Our experiments demonstrate that this method allows us to obtain guaranteed error bars with meaningful estimation even when we predict on data representing a different physical setting from that with which the model was trained on. Our study shows that irrespective of the dimensions of the output (our experiments explore models with output dimensions upwards of 20 million), we can get guaranteed coverage. We explore various methods of conformal prediction, comparing cost, performance, and associated architectural modifications. We conclude by stating that using conformal prediction we can obtain guaranteed marginal coverage across the spatio-temporal domain of interest, irrespective of the choice of model (both deterministic and probabilistic), training data and conditions.

Pathway to Addressing Climate Change

Machine-learning-based surrogate modelling is key to accelerating scientific simulation as it promises computational efficiency and allows for data-driven discovery at scale. Especially

when modelling complex systems, such as computational fluid dynamics, nuclear fusion, and weather forecasting, computational speed of scientific simulation is important; furthermore, it is increasingly crucial to provide accurate, robust, and timely uncertainty estimates. In safety-critical systems Knight (2002), it is impervious that we supplement model predictions with calibrated uncertainty estimations. This can lead to improved decision-making processes in downstream tasks. The CP framework demonstrated in this paper pushes the envelope forward in uncertainty quantification for complex scientific modelling at scale, demonstrating industry-level safety-critical applications.

Solving differential equations is a crucial tool for being able to model dynamic systems. Neural-PDE solvers offer a quick, relatively inexpensive method to solve PDEs(Yin et al., 2023), allowing us to further understand the physical system and find optimum design points(Li et al., 2023a; Shukla et al., 2024). These Neural-PDE based surrogate models offer a new pathway to solve, understand and model physical systems. But as they become more ubiquitous across various application domains, ability to verify the accuracy of their predictions becomes pressingly important.

Nuclear fusion offers a solution to low-carbon, safe, renewable, and cheap energy production. Therefore, solving nuclear fusion at a commercial scale is a key component in decarbonising hard-to-abate industries (Lerede et al., 2023). However, several challenges remain, ranging from confinement(Degrave et al., 2022), and materials (Linke et al., 2019) to mitigating disruptions (Kates-Harbeck et al., 2019). Operating on an accelerated timeline and exponential costs, iterative test-based design becomes an infeasible option. Researchers are left to solve these challenges in-silico using simulations. However, within the context of fusion modelling, at the exascale, simulation costs grow exponentially and need surrogate models capable of quicker, cheaper approximations. Neural-PDE solvers have enabled this, allowing us to solve complex multi-physical systems several orders of magnitude faster than traditional numerical solvers (Pamela et al., 2024; Carey et al., 2024). As further developments are done on these models, it is pertinent to provide rigorous methods of quantifying the uncertainty associated with these models.

Climate change has led to the observation of extreme weather events across the globe (Ebi et al., 2021). Being able to forecast weather rapidly and cheaply allows us to take proactive rather than reactive measures to these climate change-induced events. Neural weather models learnt from both simulation and observed data have emerged as cheaper and faster alternatives to traditional numerical models. However, they suffer from the limitations found within the training data, such as sparse and inaccurate observations as well as the error growth in the numerical models (Sheshadri et al., 2021). Modelling the uncertainty associated with these neural weather predictions is crucial in an operational context (Bouallègue et al., 2024). Through this work, we propose a model-agnostic method that gives calibrated error bounds for all variables, lead times and spatial locations, while not requiring any modifications to the model albeit with negligible computational costs.

2 Conformal Prediction

Conformal prediction (Vovk et al., 2005; Shafer and Vovk, 2008) answers the following question: Given some arbitrary dataset $(X_1, Y_1), (X_2, Y_2), \dots, (X_n, Y_n)$, and some machine learning model $\hat{f} : \mathcal{X} \rightarrow \mathcal{Y}$ trained on this dataset, what is the accuracy of \hat{f} at predicting

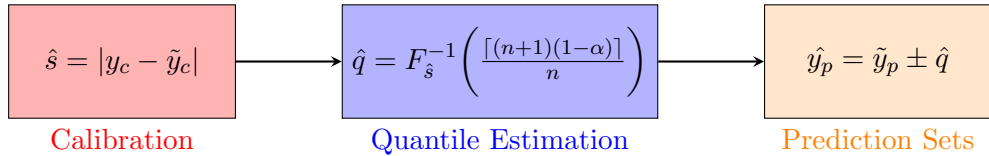


Figure 1: Inductive CP framework over a deterministic model (see AER in Section 2.2): (1) Perform calibration using a nonconformity metric (L1 error residual (AER) with \hat{s} representing the calibration scores, y_c, \tilde{y}_c the calibration targets and predictions respectively). (2) Estimate the quantile corresponding to the desired coverage from the CDF of the nonconformity scores (n represents the calibration sample size, $(1 - \alpha)$ the desired coverage, $F_{\hat{s}}^{-1}$ the quantile function applied over the inverse CDF of nonconformity scores, \hat{q} the quantile matching the desired coverage). (3) Apply the quantile to the model predictions to estimate the prediction sets (\hat{y}_p , the model predictions and \hat{q} the upper and lower bars for the predictions).

the next true label Y_{n+1} at query point X_{n+1} . CP (Vovk et al., 2005) extends the point prediction \hat{y} of \hat{f} to a prediction set \mathbb{C}^α , which is guaranteed to contain the true label Y_{n+1} with probability

$$\mathbb{P}(Y_{n+1} \in \mathbb{C}^\alpha) \geq 1 - \alpha. \quad (1)$$

CP quantifies errors in machine learning since the inequality in Equation (1) is guaranteed regardless of the selected machine learning model and the training dataset $\{(X_i, Y_i)\}_{i=1}^n$, other than that the samples used for the calibration (estimating model performance) are exchangeable (a weaker form of i.i.d.).

There have been several variants of CP since its original proposal by (Vovk et al., 2005). Inductive conformal prediction (Papadopoulos, 2008), which we pursue in this work, splits the data into a *training set* (the usual training set for the underlying ML model) and a *calibration set*, used to construct prediction set \mathbb{C}^α for each α value. The prediction sets are constructed, such that Equation (1) holds, by comparing the trained ML model to the unseen calibration data using a *nonconformity score*.

The inductive CP framework explored further in this paper follows a three-step procedure as outlined in Figure 1. Initially, we perform a calibration of the model outputs, where a nonconformity metric of the model’s performance is evaluated. This is followed by the quantile estimation, which is performed by obtaining the required quantile from the cumulative distribution of the nonconformity scores obtained in the previous calibration step. The final step involves estimating the prediction sets by applying the estimated quantile over the model predictions in the interested prediction regime.

2.1 Conformal Prediction over a Spatio-Temporal Domain

Though conformal prediction as a method of performing uncertainty quantification was introduced for fixed single-point outputs in (Vovk et al., 2005), it has been gaining popularity for usage across spatio-temporal data in the recent past (Sun, 2022). In (Stankeviciute et al., 2021), inductive conformal prediction is extended further to provide uncertainty guarantees on time-series data for RNNs, where (Xu and Xie, 2021) explores the same for dynamic

time-series forecasting. In (Xu et al., 2023), the authors explore the CP formulation to model the evolution of wildfires. The CP framework is further extended to the operator space in (Ma et al., 2024), where the authors using quantile regression learn the operator mapping to learn the upper and lower error bars of the functional space and then provide guarantees to it by using the CP framework.

2.1.1 OVERVIEW

We consider models that describe the evolution of spatio-temporal field variables defined by physical processes, such as those described in numerical PDE modelling, nuclear fusion diagnostics, and weather forecasting. Each modelling task is perceived as an initial value problem, where the calibration and prediction sets are pairs of inputs and outputs characterised by the initial condition and their respective solutions. Within the case of PDE modelling, each datapoint is a single numerical simulation, whereas for experimental modelling (such as nuclear fusion and weather), the datapoint is a single forecast driven by an initial condition.

Within our framework, we perform calibration for each cell individually, estimating the marginal coverage for each cell of the spatio-temporal tensor as demonstrated in Figure 2, i.e., the coverage is guaranteed for each cell taken individually. CP is performed across each spatio-temporal point output by the model, resulting in upper and lower coverage bands for each point. Upon calibrating for the error bars cell-wise, we averaged over each to estimate the coverage across the simulation domain. Within the estimation of the prediction sets, we don't consider the influence of adjacent field points and implicitly expect the model to extract that within the learning process. We expect the discretised spatio-temporal domain to be the same across the calibration and prediction set.

In this paper, we propose a formulation of the CP framework that provides statistically valid, dimensionality independent marginal coverage over spatio-temporal prediction models. We demonstrate the efficacy of our approach through comprehensive and rigorous experimentation across a range of spatio-temporal models, including complex multi-physics models and state-of-the-art neural weather and nuclear fusion models.

2.1.2 DEFINITION

We define a parametric model $\tilde{Y} = \hat{f}(X)$ that learns to map the evolution of an initial temporal sequence of spatial fields ($X \in \mathbb{R}^{T_{\text{in}} \times N_x \times N_y \times N_{\text{var}}}$) to a later temporal sequence of spatial fields ($\tilde{Y} \in \mathbb{R}^{T_{\text{out}} \times N_x \times N_y \times N_{\text{var}}}$). The model inputs and outputs are characterised by 4D tensors, where $T_{\text{in}}, T_{\text{out}}$ represents the temporal dimension of the initial states and forecast respectively, N_x represents the x -dimension, N_y represents the y -dimension and N_{var} the field dimension (number of modelled variables). The calibration procedure is defined as $\hat{q} = \hat{C}(\tilde{Y}, Y)$, utilising the model prediction (\tilde{Y}) and ground truth (Y) to estimate the quantile (\hat{q}) associated with the desired coverage. The operation is executed in a point-wise manner since both $\tilde{Y}, Y, \hat{q} \in \mathbb{R}^{T_{\text{out}} \times N_x \times N_y \times N_{\text{var}}}$. The quantile is further utilised (as given in Section 2.2) to obtain the lower (L) and upper error bars (U) across each of the cells to form the prediction set \mathbb{C} , where L and U have the same dimensionality as \hat{q} . At evaluation for a prediction point X_{n+1} with true label Y_{n+1} , the expectation of coverage,

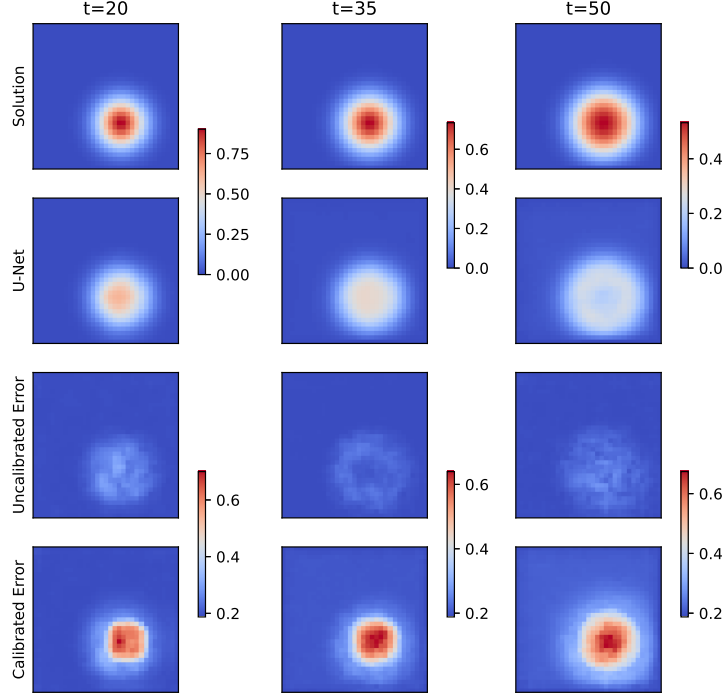


Figure 2: Cell-wise calibration of uncertainty using CP. We explore the case in Section 3.3.1, where we deploy a U-Net trained to model the wave equation in an out-of-training-distribution setting. The top row shows the ground truth, while the second row represents the prediction made by the surrogate model. The third row shows the 95% coverage (twice the standard deviation: error $\sim 2\sigma$) obtained by performing MC dropout, before performing any calibration (uncalibrated error). The uncertainty obtained post-calibration using conformal prediction is shown in the last row reflecting 95% coverage ($\alpha = 0.05$). The calibration procedure is performed cell-wise, where the error bar associated with each cell is calibrated to provide the required coverage for that cell. The uncertainties obtained from MC Dropout are unrealistically small, while the calibrated error bars provide coverage by design. Therefore, our framework helps accurately identify the regions with high levels of uncertainty, targeting the regions of higher-order dynamics.

i.e. the prediction set, is guaranteed to satisfy

$$\mathbb{E} \left[(Y_{n+1} \geq L) \wedge (Y_{n+1} \leq U) \right] \geq 1 - \alpha. \quad (2)$$

Equation (2) is statistically guaranteed to hold for each cell of the spatio-temporal tensor, provided we provide sufficient samples and exchangeability is maintained (Vovk, 2012).

2.2 Nonconformity Scores

A nonconformity score can be described as a measure of the model's performance with respect to the calibration dataset. Thus, the scores are a function of the trained model, the calibration inputs, and outputs (Angelopoulos and Bates, 2023). Nonconformity scores describe the deviation of the model from ground truth. In this paper, we focus on three methods of estimating the nonconformity scores for a model:

- **Quantile Regression (CQR):** Outlined by (Romano et al., 2019), three models are trained to perform conformal prediction. The lower and upper coverage bands are estimated by models trained to output the $100 \times \alpha^{th}$ and $100 \times (1 - \alpha)^{th}$ percentile, while the median is learned by training the model to output the 50^{th} percentile. During training the models are estimated to output the α^{th} percentile by optimising the quantile loss (Koenker, 2005). The nonconformity score measures the distance of the calibration data point from the nearest coverage band: $s(x, y) = \max\{\underline{f}(x) - y, y - \bar{f}(x)\}$. Using the upper and lower quantiles, CQR offers an initial coverage that can be adjusted and calibrated to perform conformal prediction: Using the required quantile (\hat{q}), the prediction set is obtained as $\{\underline{f}(x) - \hat{q}, \bar{f}(x) + \hat{q}\}$.
- **Absolute Error Residual (AER):** Requiring only a single model, trained to approximate the deterministic function itself, this method uses a more straightforward estimate of the model error to calibrate the coverage. nonconformity scores are estimated by taking the absolute error of the model across the labelled calibration dataset (Lei et al., 2018): $s(x, y) = |y - \tilde{f}(x)|$. Upon deriving the quantile (\hat{q}), the prediction set is obtained as : $\{\tilde{f}(x) - \hat{q}, \tilde{f}(x) + \hat{q}\}$. This method requires no structural changes to the model, and only one deterministic model is required to obtain valid prediction sets. The method uses the distribution of the absolute error residuals (AER) from the model to construct sets with the correct coverage.
- **Standard Deviation (STD):** The models are probabilistic, i.e., they predict a distribution rather than a deterministic quantity, where the outputs are characterised by a mean $\mu(x)$ and standard deviation $\sigma(x)$. The nonconformity score, $s(x, y) : \frac{|y - \mu(x)|}{\sigma(x)}$, takes into account the uncertainty of the model and conformalises it to provide validity over the predictive uncertainty ¹. The standard deviation of the output distribution provides estimates of the error bars and; thus, it is an initial measure of the coverage, which can be adjusted to ensure the correct coverage using conformal prediction. Upon deriving the quantile (\hat{q}), the prediction set is obtained as :

1. If the choice of the model is not probabilistic in itself, we will have to modify the model with changes to architecture or introduce sampling strategies to output a distribution.

$\{\mu(x) - \hat{q}\sigma(x), \mu(x) + \hat{q}\sigma(x)\}$. To do CP using a probabilistic model, we modify our networks to behave in a probabilistic manner through architectural modifications or changing the training regime.

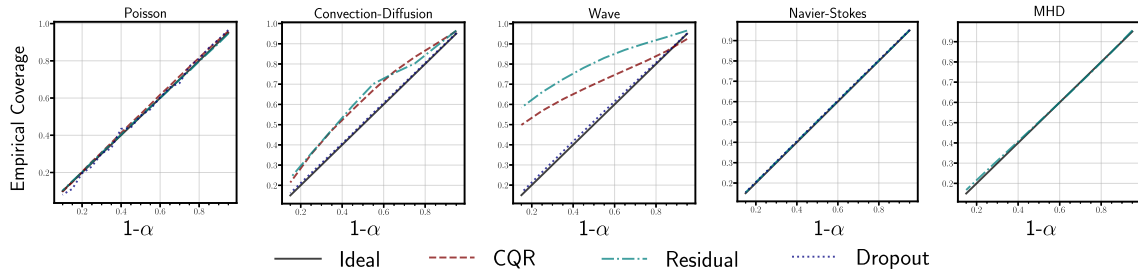


Figure 3: Validation plots indicating the coverage guarantee detailed in Equation (1) obtained by CP across experiments, models, and calibration methods. The average empirical coverage guaranteed by CP is given on the y -axis (ranging from 0 to 1, with 1 representing 100% coverage), while the coverage, which we calibrate for, is represented on the x -axis. Validation plots are shown for the four PDEs we focus on in this paper. We obtain guaranteed coverage for all calibration methods in all our experiments.

Figure 3 illustrates how these nonconformity scores can help obtain guaranteed coverage, across all modelling scenarios considered in the paper (more details on them in Section 3). The coverage provided across the nonconformity scores may vary, but the CP formulation ensures the validity of the error bars. Irrespective of the choice of the nonconformity score, we obtain near-to-ideal coverage for the prediction following the inequality found within Equation (1). Since coverage is guaranteed in the framework, the choice of the nonconformity score is often undertaken considering other aspects such as architectural modifications, calibration time, and cost of obtaining additional data.

The coverage can be empirically tested using a validation dataset. Initially, we perform calibration of the model, which is followed by computing the prediction set \mathbb{C}^α using the calibrated metrics, and eventually computing the empirical coverage

$$\mathbb{P}(Y_{\text{val}} \in \mathbb{C}^\alpha) \approx \frac{1}{n_{\text{val}}} \sum_{i=1}^{n_{\text{val}}} I_{\mathbb{C}^\alpha}(Y_i), \quad (3)$$

where $I_{\mathbb{C}^\alpha}$ is the indicator function of the prediction set associated to α prediction set. If the estimated probability is greater than $1 - \alpha$, the α prediction sets correctly capture the true coverage.

(Vovk, 2012) shows that the empirical coverage is distributed as

$$\frac{1}{n_{\text{val}}} \sum_{i=1}^{n_{\text{val}}} I_{\mathbb{C}^\alpha}(Y_i) \sim \text{beta}(n_{\text{cal}} + 1 - l, l), \quad (4)$$

where $l = \lfloor (n_{\text{cal}} + 1)(1 - \alpha) \rfloor$.

CP provides prediction sets at any α -level, which coverage may be empirically computed for. This is visualised in Figure 3, where the empirical coverage is plotted against the $1 - \alpha$

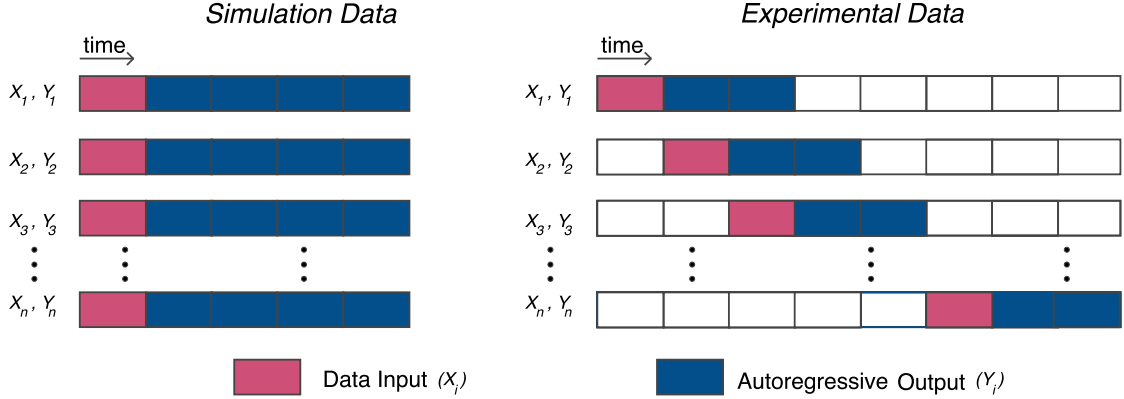


Figure 4: Exchangeable input-output pairs: Within the surrogate models for simulation, the calibration dataset is composed of several simulations, run with different initial conditions, forecasting across the same time domain. Within the surrogate models used for experimental data, exchangeable input-output pairs are formed from within a single experiment, but the IC is taken at several points within the experiment, forecasting across the same time domain.

target coverage from CP. The straight line shows the ideal scenario where the empirical coverage exactly matches the predicted coverage, i.e., the inequality in Equation (1) is an equality. Figure 3 serves as a validation plot of our ‘‘conformalised’’ surrogate model, where we use an unseen validation dataset to empirically check the true coverage (using Equation (3)) against the predicted coverage for CP, validating Equation (1) for each α -level. Figure 3 shows that we obtain guaranteed coverage across a previously unseen prediction set irrespective of the choice of calibration method across all our experiments.

2.3 Exchangeability Assumptions

Throughout the experiments considered in this paper, surrogate modelling of spatio-temporal data is treated as an initial value problem (IVP). To map the evolution of the system under study, the surrogate model takes in the initial state(s) of the system and evolves the system autoregressively in time. By treating the modelling task as an initial value problem, each input-output pair (X_i, Y_i) from the calibration and the prediction dataset is assumed to be exchangeable. The initial condition associated with each IVP is sampled i.i.d. from a distribution characterising the possible (large) range of interested initial conditions for the prediction task. The assumption relies on the further caveat that is outlined in Section 2.1.2, the structure of each spatio-temporal output is maintained. The CP framework requires exchangeability not just across the calibration data but across the prediction data as well (Angelopoulos and Bates, 2023). To maintain exchangeability across the calibration and prediction datasets, we have to ensure that the full spatio-temporal context window across them remains the same and assume that they arise from the same distribution. The exchangeability assumption is more complex in the case of experimental data, and we discuss this further in Section 3.7 and Section 3.8.

In Section 3 we consider two types of experiments: surrogate modelling over simulations and experimental data. Within the simulation context (Section 3.1 to Section 3.6), the

modelling task takes in the initial state of the system at $t = 0$ and then evolves the system (autoregressively or in one-shot) to time $t = T$. The model always starts at the initial condition(s) of the simulation and maps till a fixed time state T . Whereas in those modelling experimental data (Section 3.7 and Section 3.8) the modelling task takes the system at $t = T$ to $t = T + \Delta T$. The starting time instance (initial condition) T changes in each exchangeable data pair but the model evolves it for a fixed time duration of ΔT . Within the simulation setup, it is easier to gather data as required, exploring a data-abundant scenario. In the case of real-world experiments, data is scarce and we had to rely on breaking down available data to obtain the calibration data. We characterise this difference in how the exchangeable pairs are conceived for both the simulation and experimental data in Figure 4.

3 Experiments

To evolve spatio-temporal data describing physical systems, we train several surrogate models using simulation data built from numerical solvers designed for the PDE of interest. Across our experiments, we choose different kinds of surrogate models. Multi-Layer Perceptrons (MLPs) (Haykin, 1994), U-Nets (Ronneberger et al., 2015), Fourier Neural Operators (FNOs) (Li et al., 2021), vision transformers (Yin et al., 2022b), and graph neural networks Scarselli et al. (2009) are utilised. These networks are commonly used as surrogate models for challenging systems in physics and engineering (Mánek et al., 2023; Gupta and Brandstetter, 2023; Wen et al., 2023; Geneva and Zabaras, 2022; Sanchez-Gonzalez et al., 2020).

MLPs have been used as surrogates for modelling wind turbine blades (Lalonde et al., 2021), classifiers for high-energy physics (Baldi et al., 2016), and for designing fusion reactors (Mánek et al., 2023). U-Nets and FNOs are structured as neural-PDE based approximators that can learn across the operator space rather than the function space of the mapping. They find utility in designing surrogates for fluid dynamics (Gupta and Brandstetter, 2023), studying carbon capture and mitigation (Wen et al., 2023), weather modelling (Kurth et al., 2023) and modelling plasma evolution within a nuclear fusion device (Gopakumar et al., 2023). Transformers have found application in PDE solving (Li et al., 2023b) and weather modelling (Nguyen et al., 2023). GNNs have been deployed to model Lagrangian dynamics of a PDE and in solving particle-in-cell scenarios (Brandstetter et al., 2022); they also have been applied to weather forecasting (Lam et al., 2023).

The MLP represents a fully connected neural network. The U-Net is a fully convolutional autoencoder (Hinton and Salakhutdinov, 2006) with skip connections (He et al., 2016; Takamoto et al., 2022). The FNO is an operator learning method that learns the kernel integration across the Fourier space (Li et al., 2021). A vision transformer is an attention-based model that learns spatio-temporal rollouts through sequence patching of the spatial outputs and auto-regressive rollouts. Graph neural networks deploy message-passing across nodes representing the spatio-temporal information to model the evolution of a physical system. Depending on the specific experiment we adjust the model setup to either do a one-step forward-in-time mapping or perform an auto-regressive time roll-out over multiple time steps. All models were trained on an NVIDIA A100 GPU, while the calibration and estimation of prediction sets were done on a standard laptop.

Table 1: Coverage comparison of all models ($\alpha = 0.1$). ‘Uncalibrated’ refers to coverage before performing CP (not available for AER method), and ‘calibrated’ is coverage after CP. Across our experiments, models, and calibration methods, we obtain nearly perfect coverage. Tightness is measured as the average width of the error bars across each cell of the spatio-temporal tensor in normalised units. * represents experiments where the training set and calibration set are from a different distribution. ‘PT’ refers to the evaluation on the pre-trained model, and ‘FT’ refers to those over the fine-tuned models.

Case	Model	Output Dims	Method	Uncalibrated (%)	Calibrated (%)	Cal. Time (s)	Tightness
1D Poisson	MLP	32	CQR	94.61	90.01	0.0035	0.012
			AER	-	90.05	0.0030	0.002
			STD	97.5	90.85	0.133	0.025
1D Conv-Diff	U-Net	2,000	CQR	25.53	93.05	19.70	0.314
			AER	-	92.60	8.30	0.266
			STD	88.43	90.29	88.15	0.164
2D Wave	U-Net	32,670	CQR	96.95	89.21	8.40	0.132
			AER	-	94.91	3.52	0.013
			STD	4.45	90.30	39.51	0.012
	FNO*	65,340	AER	-	89.24	34.18	0.330
	STD	32.81	89.83	462.0	0.669		
2D Navier-Stokes	FNO*	40,960	AER	-	90.08	4.83	0.381
			STD	7.52	90.27	64.75	0.448
2D MHD	FNO	1,348,320	AER	-	90.18	359.12	0.039
2D MHD	ViT* (PT)	313,344	AER	-	89.95	2980.50	0.062
	ViT* (FT)		AER	-	89.78	2078.50	0.015
2D Camera	FNO	2,867,200	AER	-	91.28	293.62	0.131
2D Weather (Limited Area)	GNN	20,602,232	AER	-	91.09	229.23	1.13
	GNN		STD	74.62	91.08	309.55	0.96
2D Weather (Global)	GNN	12,777,600	AER	-	90.03	366.41	1.34
	GNN		STD	71.22	89.88	400.57	1.28

Table 1 forms the centrepiece of our work. The table shows the coverage obtained when predictions are calibrated for $\alpha = 0.1$ (90% coverage) across our experiments utilising the three different calibration methods (nonconformity scores) discussed in Section 2.2. For CQR and STD, we additionally show the coverage before performing CP, as these methods have initial uncertainty estimates, which are calibrated to ensure guaranteed coverage. This is labelled as ‘uncalibrated’ in Table 1. For each experiment, an adequate pre-trained surrogate model is developed or chosen. The CP framework is performed over its output dimensions, observing near-to-ideal coverage. The “tightness of fit” depends on the choice of *nonconformity score*. The tightness is taken to be the width of the calibrated error bars, averaged across each cell of the tensor. In most experiments we find the AER to offer the best fit, however, STD is a close second.

Demonstrations of the CP formulation for estimating marginal coverage as given in Section 2.1.2 for each experiment, irrespective of the complexity and case-setting follow the structure outlined below.

CP Framework: Experiment Structure

- 1: Generate training data (if training is involved)
- 2: Pre-train / fine-tune surrogate model
- 3: Generate calibration dataset / Use fine-tune dataset
- 4: Obtain error bars using the Conformal Prediction framework
- 5: Add the error bars to the prediction datasets
- 6: Evaluate coverage

3.1 1D Poisson Equation

The Poisson equation is a generalisation of the Laplace equation. It relates the Laplacian of a field to the distribution of the sources/sinks in the field (Hackbusch, 2017). The elliptic PDE models various physical phenomena, such as electrostatics, gravitation, and fluid dynamics. The Poisson equation is a steady-state problem (spatial-only), where the interest lies in mapping the initial distribution of the field to its final state. The state is given along the x-axis, discretising the domain $[0, 1]$ into 32 uniform grid points. An initial dataset consisting of 5000 simulation data points is generated and used to train an MLP. Another 1000 data points are generated to calibrate the trained model using the CP framework along with another 1000 for validating the procedure. The training data, calibration, and validation datasets are sampled from the same distribution within this case. Further details about the physics, data generation strategies and model training can be found in Appendix A.

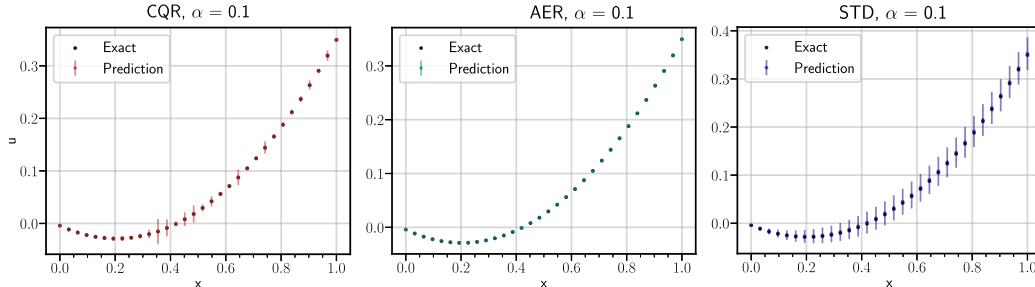


Figure 5: Error bars obtained by performing CP over the MLP modelling the Poisson equation for the three different methods. Considering the simple setup of the problem, the model fits to near perfection, leading to tighter fits, with small error bars characterising the calibrated bounds.

Multiple MLPs are trained to demonstrate the efficacy of different nonconformity scores while using the CP framework. To perform the CQR, three models are trained, modelling the 5th, 50th and 95th quantile, while for AER a single model is trained to output the evolved field using an L1-norm. For CP using STD, an MLP with dropout is trained to obtain a probabilistic model that learns the distribution of the evolved state. The performance comparison of each nonconformity score is laid out in Table 1.

Figure 5 visualises the $\alpha = 0.1$ prediction sets (90% confidence intervals) of CQR (left), AER (centre), and STD (right). Considering the simplicity of the physical dynamics, the

MLP learns the mapping to near perfection leading to tighter uncertainty estimates, with a narrow set characterising the uncertainty.²

3.2 1D Convection-Diffusion Equation

Moving further up in complexity from a steady-state (spatial-only) to a dynamical case (spatio-temporal), consider the convection-diffusion equation in one dimension. As a combination of a parabolic and hyperbolic PDE, the equation is crucial in modelling transport phenomena in various science and engineering applications (Chandrasekhar, 1943). Following the schema laid out in Algorithm : CP Structure, an initial training dataset of 3000 simulations is generated by sampling the initial conditions and the physical factors of the PDE (diffusion coefficient and convection velocity) from a hypercube. A 1D U-Net is trained as the surrogate to model the spatio-temporal evolution given by the convection-diffusion equation. The model takes in the first 10 time instances to map to the next 10 time instances. The physics, sampling strategies, and model details can be found in Appendix B. The calibration and validation datasets are generated from a slightly shifted domain space as that used for training, where the simulation physics is modelled with less diffusion and more convection. This helps to explore a scenario of deploying a pre-trained surrogate model on an out-of-training-distribution setting.

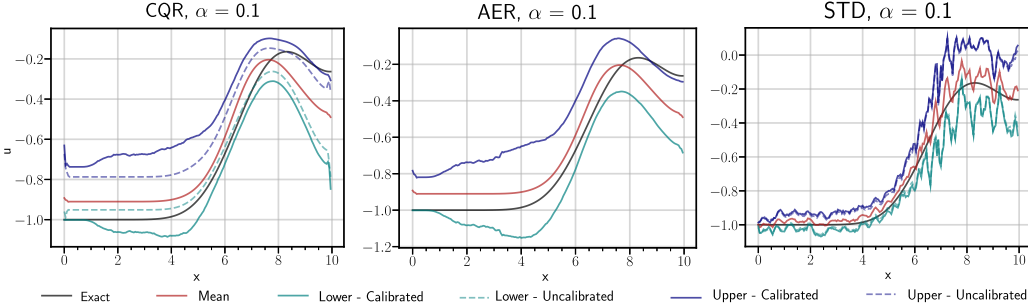


Figure 6: Calibrated lower and upper bounds of the model output for the 1D convection-diffusion equation with $\alpha = 0.1$ providing 90% coverage. The plots show the field distribution across the x -axis at the final time instance $t = 0.1$. When the uncalibrated coverage is too constrained (as with CQR), CP helps widen it to provide the required coverage. In the case of STD, note that for models with lower dimensionality, the sampled uncertainty is calibrated moderately well before performing CP over it.

In Figure 6, we calibrate the model with a dataset that characterises less diffusion and more convection than in the training dataset. The training dataset had instances of the PDE with diffusion coefficient sampled from the domain $D \in [\sin(x/2\pi), \sin(x/\pi)]$ and convection velocity $c \in [0.1, 0.5]$. The calibration and prediction dataset was sampled with diffusion coefficient $D \in [\sin(x/4\pi), \sin(x/2\pi)]$ and convection velocity $c \in [0.5, 1.0]$; see Appendix B for more details. Even when tested on this data from a new distribution, we obtain valid prediction sets with guaranteed error bars. The coverage offered by each

2. A fully reproducible script demonstrating the CP framework over the Poisson equation can be found at https://github.com/gitvicky/Spatio-Temporal-CP/blob/main/Poisson/Poisson1d_NN_CP.py.

calibration methodology is given in Figure 3. Note that we obtain guaranteed coverage across all values of α . However, the estimation of coverages using CQR and AER tends to be overly conservative as seen in Figure 3, which we believe is observed due to the overfitting of the model to the simple modelling task. In Figure 6, we show the upper and lower bands prescribing the coverage (both calibrated and uncalibrated where available) along with the model prediction and the exact solution. With both CQR and STD, the uncalibrated coverage is below the expected coverage, but using CP we can obtain the desired coverage. The lower and upper bounds provided by CP ensure that at least 90% of the exact solution is covered by them. The performance comparison of each nonconformity score is laid out in Table 1.

3.3 2D Wave Equation

The wave equation is a second-order hyperbolic partial differential equation that describes the propagation of waves through a medium with numerous applications in acoustics, optics and quantum mechanics (Tipler, 2008). The experiment focuses on the spatio-temporal dynamics of a 2D Gaussian under the constraints of the wave equation. The detailed description of the physics, the numerical solvers, and the data generation strategy are given in Appendix C. To build the pre-trained model to evaluate the CP framework, initially, a training dataset of 500 simulations is generated by varying the parameterisation of the initial condition, i.e., the amplitude and position of the Gaussian. The data is used to train a U-Net and an FNO that models the temporal evolution of the wave dynamics.

3.3.1 U-NET

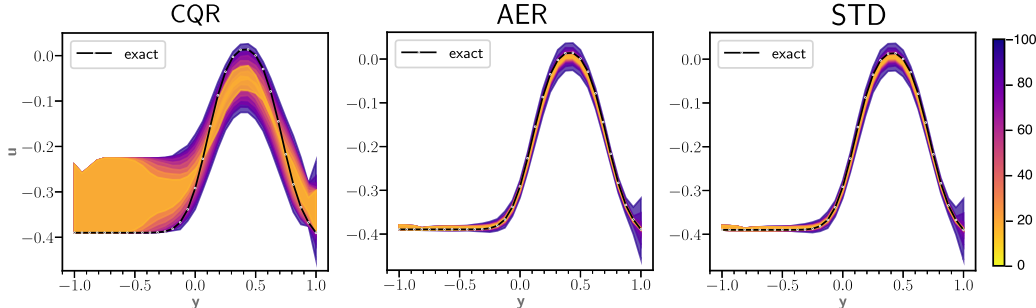


Figure 7: Calibrated prediction sets obtained by performing conformal prediction with the three nonconformity scores mentioned in Section 2.2 for the 2D wave equation. The color bar depicts the coverage (in %) provided by each prediction set, characterised by the $1 - \alpha$ value. Each figure shows a slice of the prediction set and exact inference value taken along the y -axis for the final time instance of the prediction. The exact numerical solution (black with white markers) can be seen to fit up to the coverage offered by the prediction set.

U-Net is designed to perform a single feed-forward map, taking in 20-time instances of the field to produce an output of shape $[30, 33, 33]$, characterised by 30-time instances across a 33×33 spatial domain. A calibration and validation dataset comprising 100 simulations each is generated from the same distribution as that of the training data to evaluate CP

for the wave equation. Coverage is estimated at each point in the output tensor as given in Section 2.1.2.

Comparing the different methods used for CP (in Figure 3 and Table 1), we see that the AER method is the least computationally intensive and offers valid coverage. This is further accentuated by Figure 7, where the tightness of the fit and the coverage obtained by performing CP at various values of α is given. All methods provide valid coverage in tandem with the ideal coverage as expected by Equation (1), where those using quantile regression and AER errors provide overly conservative error bars. This is expected as Equation (1) offers an inequality, offering wide predictive sets for the specific value.

In Figure 7, we take the slice along the y -axis of the prediction sets at various α levels to visualise the uncertainty of the predicted field for that slice. The slices represent the variation of the field along the y -axis for the final time instance of the prediction. Figure 7 shows that the tighter fits are obtained using the AER and STD methods, where the quantile regression fails to provide a tight fit although it provides good coverage.

To further iterate the impact of the CP framework as a method of uncertainty quantification, we further generate calibration and validation data, but this time from a different physical model. The newer datasets are sampled by solving the wave equation with wave velocity at half the speed of that used for the training data. This allows us to further benchmark the CP formulation in the paper in cases where the calibration and prediction regimes are outside of the training distribution. As given in Figure 2, when utilised outside of the training domain, the uncertainty captured by dropout (STD) fails to capture the modelling failure. However, by calibrating the uncertainty using the CP framework, it can capture the model’s (in)capabilities with statistical guarantees, irrespective of the training conditions of the pre-trained model. This becomes particularly important when we consider the utility of the surrogate model in out-of-training-distribution scenarios, where we will need more data to fine-tune the network.

3.3.2 FNO

Furthering the experiment’s complexity, FNOs are trained in an autoregressive framework to model the spatio-temporal evolution of the wave. The autoregressive model takes in the first 20 time instances to output the next 10 time instances, further unrolled for the next 60 time instances. We perform conformal prediction across the entire time rolled-out output of shape $[60, 33, 33]$. Since the FNO offers the best performance when trained using a relative LP norm, we did not perform CQR for experiments using the FNO.

While performing conformal prediction over the FNO, we also demonstrate its utility in obtaining statistically guaranteed coverage for inference over a physics scenario different from the one on which the FNO was trained on as mentioned in the earlier section (also see Appendix C). The FNO is applied in the same in-distribution and out-of-distribution setting as the U-net. Through this, we demonstrate the validity of the error bars even when predicting out-of-training-distribution data.

Figure 23 (in the appendix) shows that we obtain guaranteed coverage for predictions across calibration methods, even when tested outside the training distribution. As shown in Figure 8, the CP framework provides valid error bars for the desired coverage, irrespective of the training conditions. The only criterion that needs to be met is that the prediction

regime and the calibration regime are exchangeable. The inductive CP framework can provide valuable uncertainty quantification, even when deployed to solve for those unseen sets of solutions. Furthermore, FNO offers a tighter fitting coverage than the U-Net used for the wave equation; see Figure 3.

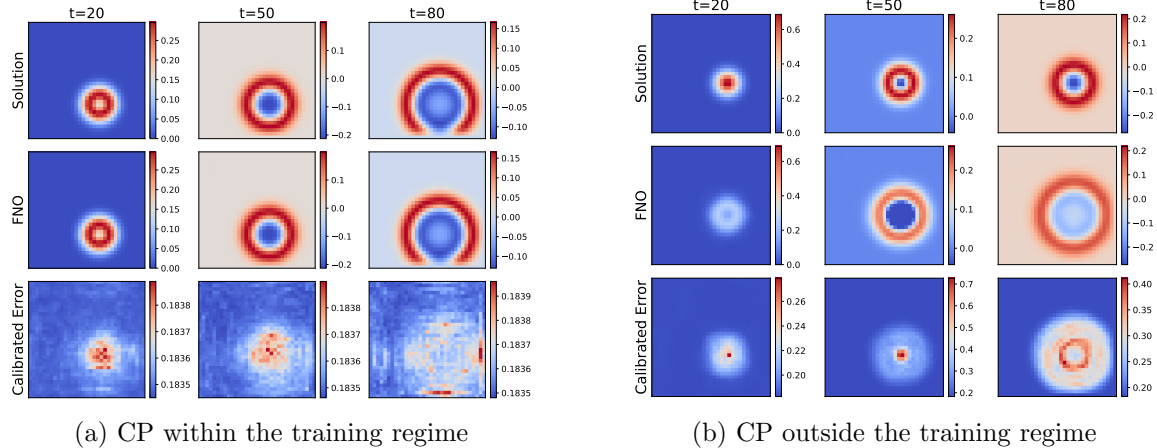


Figure 8: Visualising the errors obtained using the CP framework for an auto-regressive FNO within (Figure (a)) and outside the training distribution (Figure (b)). In both figures, the top row represents the numerical solution of the wave equation, the FNO prediction in the middle row and the calibrated error for 90 % coverage.

3.4 2D Navier–Stokes Equations

The 2D Navier–Stokes equations are a family of PDEs that describe the motion of viscous fluids. The equations establish a mathematical model for the conservation of mass, momentum, and energy in a fluid flow. Considering its complexity and strong non-linearity the Navier–Stokes equations are solved using computational fluid dynamics (CFD). Neural-PDEs have emerged as a suitable method to assist complex CFD simulators to solve the Navier–Stokes equations at scale (Azizzadenesheli et al., 2024). Within this experiment, an FNO is trained to model the evolution of vorticity as described in the original FNO paper (Li et al., 2021). Further descriptions of the physics formulation, datasets and training can be found in Appendix D. The model was trained from simulations with viscosity $\nu = 1e - 3$ and then calibrated to form the prediction set for viscosity $\nu = 1e - 4$. The datasets were gathered from the original FNO paper Li et al. (2021). The coverage obtained across the out-of-distribution prediction sets can be seen in Figure 3. We modify the FNO in (Li et al., 2021) with dropout layers, to train a probabilistic neural operator. As shown in Figure 9, deploying the CP framework across the probabilistic outputs to be further calibrated to obtain guaranteed coverage.

3.5 2D Magnetohydrodynamics

Magnetohydrodynamics (MHD) governs the evolution of a plasma state within a fusion device, such as a Tokamak. It is characterised by the coupling of Navier–Stokes equation of

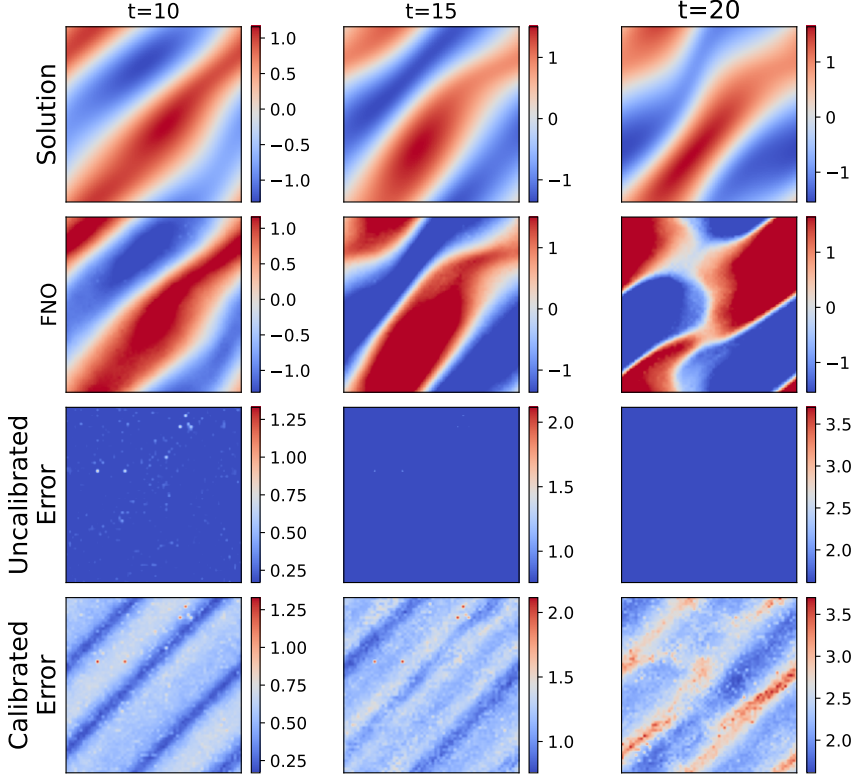


Figure 9: Calibrating the uncertainty captured by using MC dropout (STD) within the FNO in modelling out-of-distribution data for the Navier–Stokes case. The top row shows the ground truth, the second row the output of the FNO, the third row the error (taken as the standard deviation here) captured by the probabilistic FNO, and the final row shows the calibrated error obtained using the CP framework over the probabilistic outputs showing 67 % coverage.

fluid dynamics and Maxwell’s equations of electromagnetism (Bellan, 2006). The evolution of MHD fields involves modelling multi-physics systems with coupled variables (θ) that are integrated together. We model the evolution of multiple plasma blobs in a non-uniform temperature field with a reduced-MHD model as described by (Hoelzl et al., 2021). The model governs the spatio-temporal evolution of the density (ρ), electrostatic potential (Φ) and temperature (T) within a simple circular geometry, modelled in the toroidal coordinates R and Z . The full description of the MHD physics we are interested in modelling is provided in Appendix E.

The dataset and the trained model were taken from (Gopakumar et al., 2024). The data was constructed by running simulations of the reduced-MHD cases using the code JOREK (Hoelzl et al., 2021). The physics of the equation was kept stationary throughout the campaign; however, the initial conditions that characterise the blobs were changed within each simulation (see Appendix E). A total of 2000 simulations/data points were generated, out of which 1000 were used for training, 500 for calibration and 500 for validating the prediction sets.

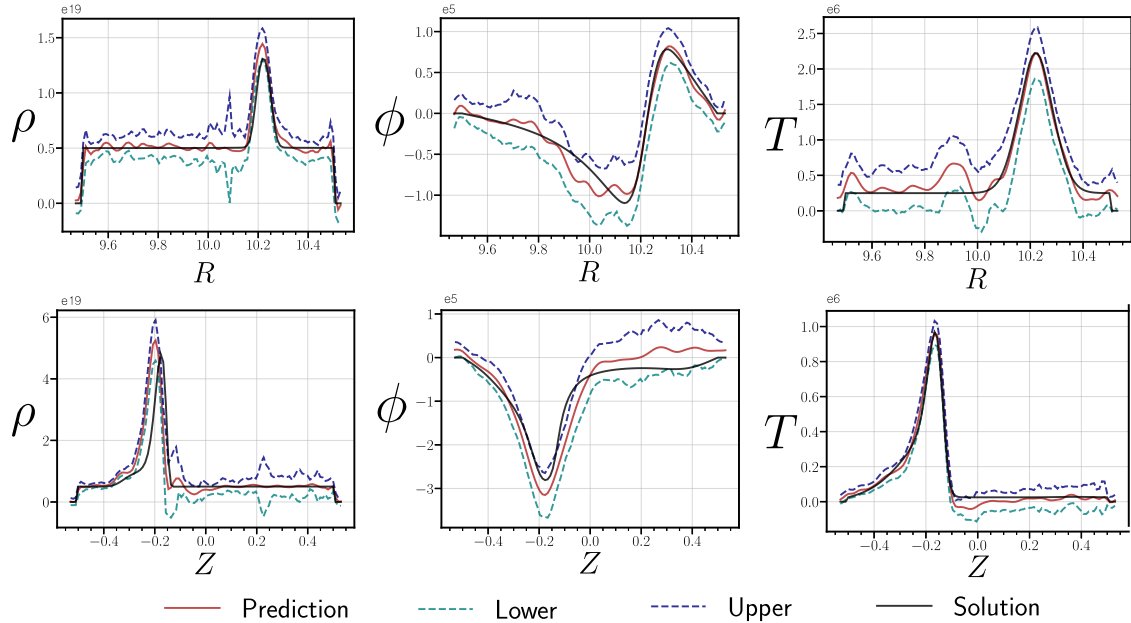


Figure 10: Spatial slice plots showing 90 percent coverage ($\alpha = 0.1$) over the multi-variable FNO predictions, calibrated using conformal prediction. The figures represent the spatial distribution of the plasma density ρ (left column), electrostatic potential Φ (middle column) and plasma temperature T (right column) along the axes as obtained from the numerical solution, FNO and the upper and lower bands at the 20th timestep. The top plots portray the field distribution along the R -axis and the bottom plots the field distribution along the Z -axis. Across the dimensions of the output, we can obtain valid error bars, fitting within the desired coverage for our surrogate model.

Considering the complexity of the system, we deploy a multi-variable FNO (as demonstrated in (Gopakumar et al., 2024)) to learn the correlated dynamics of all of the field variables associated with the reduced-MHD setting. The model is trained and deployed in an autoregressive framework, using the first 10 time instances to output the next 5 time instances, recursively continued until the model predicts the 50th time instance. We perform conformal prediction over the entirety of the spatio-temporal domain that is outputted by the FNO, obtaining prediction sets for each point within that 4D space characterised by field variables across the spatio-temporal domain. Considering the size of the model (see Appendix E), we restrict ourselves to performing conformal by AER. Figure 10 shows the error bars obtained by performing CP over the MHD modelled by the multi-variable FNO. The Figure 10 shows the slice plots along the R and Z axes of the prediction along with the error bars for 90% coverage. We obtain guaranteed coverage (see Figure 3) over the model predictions even when deployed on a large model, such as the multi-variable FNO (9,448,805 parameters), producing high-dimensional outputs (1,348,320 dimensions). Figure 10 shows the error bars that bound the model prediction to the peaks in density, temperature and electric potential characterised by the plasma blobs. The upper

bounds obtained by CP allow us to understand the distribution of model outputs across the domain of interest, indicating the confidence associated with the prediction.

3.6 Foundational Physics Models

Foundation models (Bommasani et al., 2022) capable of performing multi-task modelling across a range of PDE-related tasks have been developed in the recent past (McCabe et al., 2023; Alkin et al., 2024; Hao et al., 2024; Rahman et al., 2024). These models rely on deploying novel transformer-based architectures that deploy an attention mechanism across the spatio-temporal domain to pre-train across various families of PDEs, allowing complex multi-physics scenarios to be modelled. The underlying principle relies on the idea that PDEs describing various physical systems, share similar differential operators. The models have shared embeddings across the variables to characterise the different physical operators, such as diffusion or convection. This allows them to learn the global behaviour governing different PDEs, leaving the local features to be learnt in the fine-tuning stage Alkin et al. (2024).

As these models scale and find further application across a range of domains, it becomes increasingly critical to quantify the uncertainty associated with the model predictions. Being pre-trained on diverse PDE datasets, these models often find applications in similar tasks. Considering the complexity of scale and the importance of the task, it is hard to validate the utility of these pre-trained models in an application without being able to provide UQ estimates that can be guaranteed. The same extends to fine-tuned models, trained for a specific downstream application. By performing conformal prediction across the model outputs at each space, we are able to validate the model performance for a specific application. CP relies on requiring ground truth data to help provide statistical validity, enforcing some computational effort in generating the numerical data. However, in the case of the application of a fine-tuned model for a specific application, calibration data already exists as the fine-tuning data. The central utility of this CP framework within the domain of surrogate modelling becomes clearer when extended to the fine-tuning setting where the prediction domain is the same as the training domain, reducing the need for further collection of data for calibration.

Within this experiment, we restrict our focus on applying the CP framework across one of the early attempts at a Foundational Physics Model, demonstrated in (McCabe et al., 2023). The authors modify the architecture of an adaptive vision transformer (AViT) (Yin et al., 2022a) with shared embedding and normalisation strategy across the variable space. The model uses an AViT backbone which attends over the space and time axis sequentially. The model is trained autoregressively to output the next time instance of the field(s) across the spatial domain. For further details on the model architecture, training setup, and the datasets used for pre-training, we refer to the original paper (McCabe et al., 2023).

3.6.1 PRE-TRAINED MODEL: ZERO-SHOT LEARNING

Within the first experiment, the efficacy of the pre-trained foundational physics model to evolve the unseen physics is explored in conjunction with the formulated CP framework. The largest Multi-Physics Pre-trained (MPP-AViT-L) from (McCabe et al., 2023), consisting of 409 million parameters, is tested on the MHD dataset as detailed in Section 3.5. The

MPP-AViT-L model is pre-trained to model across a range of equations: shallow-water, diffusion-reaction and Navier–Stokes equations, where the model learnt to model densities, velocities and pressure formulations. Thus, we isolate the density fields from the MHD data to perform inference over the MPP-AViT-L model. The model is structured to take in the first 16 time steps for each simulation and then output the next time step. This procedure is autoregressively continued until the 50th time instance.

Analysing Figure 11, even for a pre-trained model with no exposure to MHD information within its training regime, it performs moderately well in mapping the evolution of plasma density as the blobs move radially outward in time. The major features of the density of the plasma blobs are captured, missing some of the finer, more defining features. We also notice the emergence of patch-based features which is an artefact of the model as highlighted in (McCabe et al., 2023). To estimate the uncertainty of the prediction, we deploy the CP framework. Following the schema laid out in Algorithm : CP Structure, calibration is performed using the AER nonconformity score using 1000 calibration data points and used to obtain prediction sets. The bottom row of Figure 11 demonstrates 95 % coverage (width of the error bars) obtained by deploying the CP framework, being able to bound the model performance with coverage guarantees. Note that the errors obtained from the CP framework (\hat{q}) are a function of the calibration data and remain the same for the prediction set.

3.6.2 FINE-TUNED MODEL

The next iteration involves fine-tuning the MPP-AViT model on the density fields from the MHD dataset to create a foundation model well-versed in magnetohydrodynamics found within the core of a Fusion reactor. We fine-tune the tiny version of the foundational physics model (MPP-AViT-Ti) using 3/4 of the available data for training and calibration. The remaining 1/4 is used for evaluation and obtaining the prediction sets. Within the fine-tuning context, the training data doubles up as calibration data. The intention of fine-tuning is often to bring a certain data regime within the distribution of the model, hence the fine-tuned model’s performance is only of interest within the new domain. This allows us to care about performance in the same distribution as that of the fine-tuning data, allowing us to use the same data to calibrate the model as we are only interested in performance within the same domain. Since the objective of fine-tuning is to align a model with a specific task, the usage of training data as calibration data is well justified. From Figure 12, we notice that fine-tuning the foundation model on the MHD model resulted in a significant improvement in performance as compared to the previous instance of zero-shot learning.

Though the CP framework offers a coverage guarantee (see Appendix F), the calibrated error values end up being more general, characterising the global dynamics and uncertainties. This arises due to the deterministic nature of the model, not providing input dependence to the prediction sets. For a considerably well-fit, as seen in Figure 12, only the global uncertainties are captured.

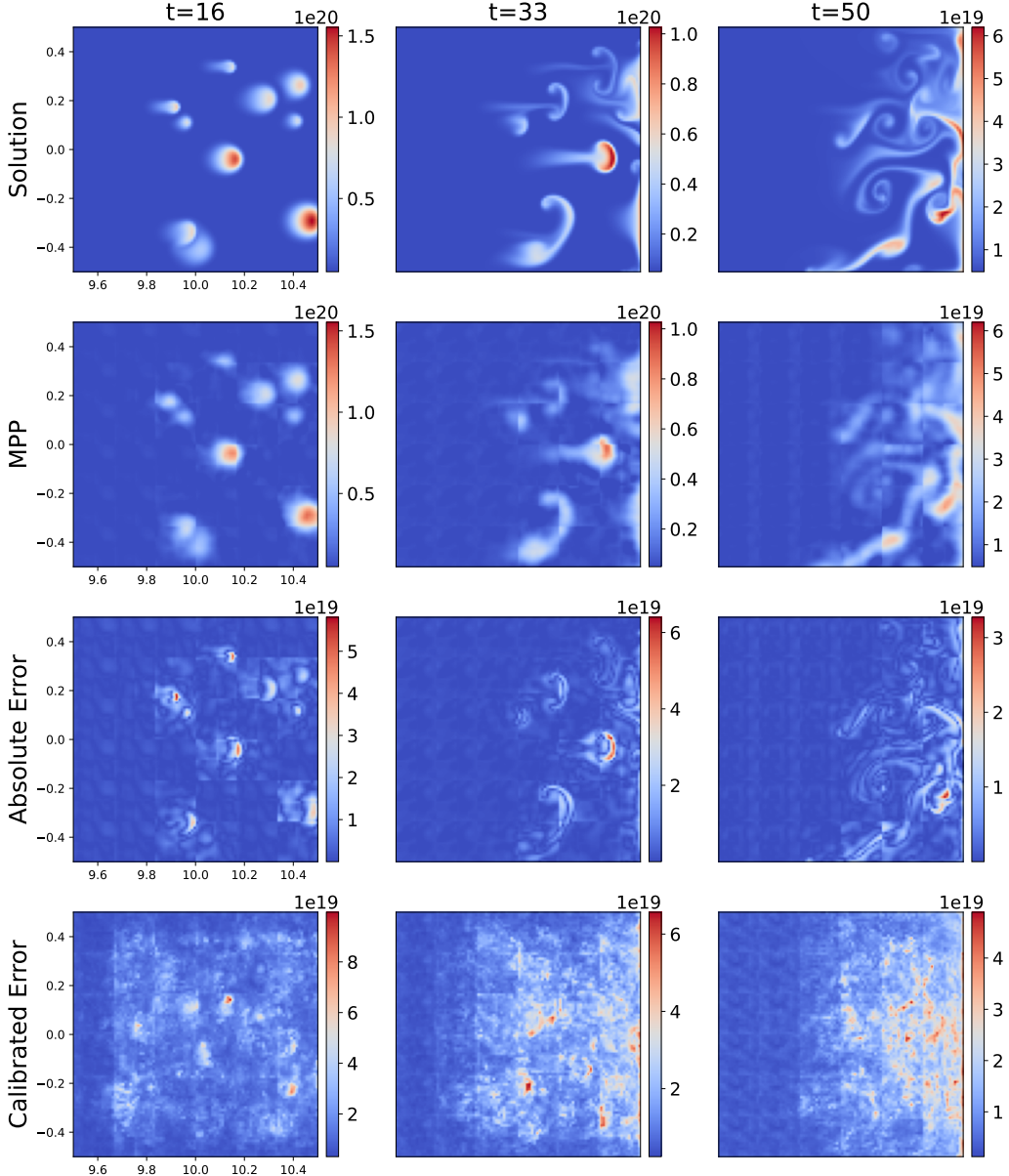


Figure 11: Performance of the MPP-AViT model in modelling MHD density (out-of-training-distribution data). The top row shows the numerical solution, the second row shows the model output, the third row shows the absolute error, and the bottom row shows the calibrated error (width of the error bars) providing 95% coverage.

3.7 Neural Weather Prediction

In addition to surrogate models of systems described by explicit PDEs, the proposed methodology is also applicable to more general machine learning models describing physical processes. To demonstrate this, we here study the use of CP for data-driven weather

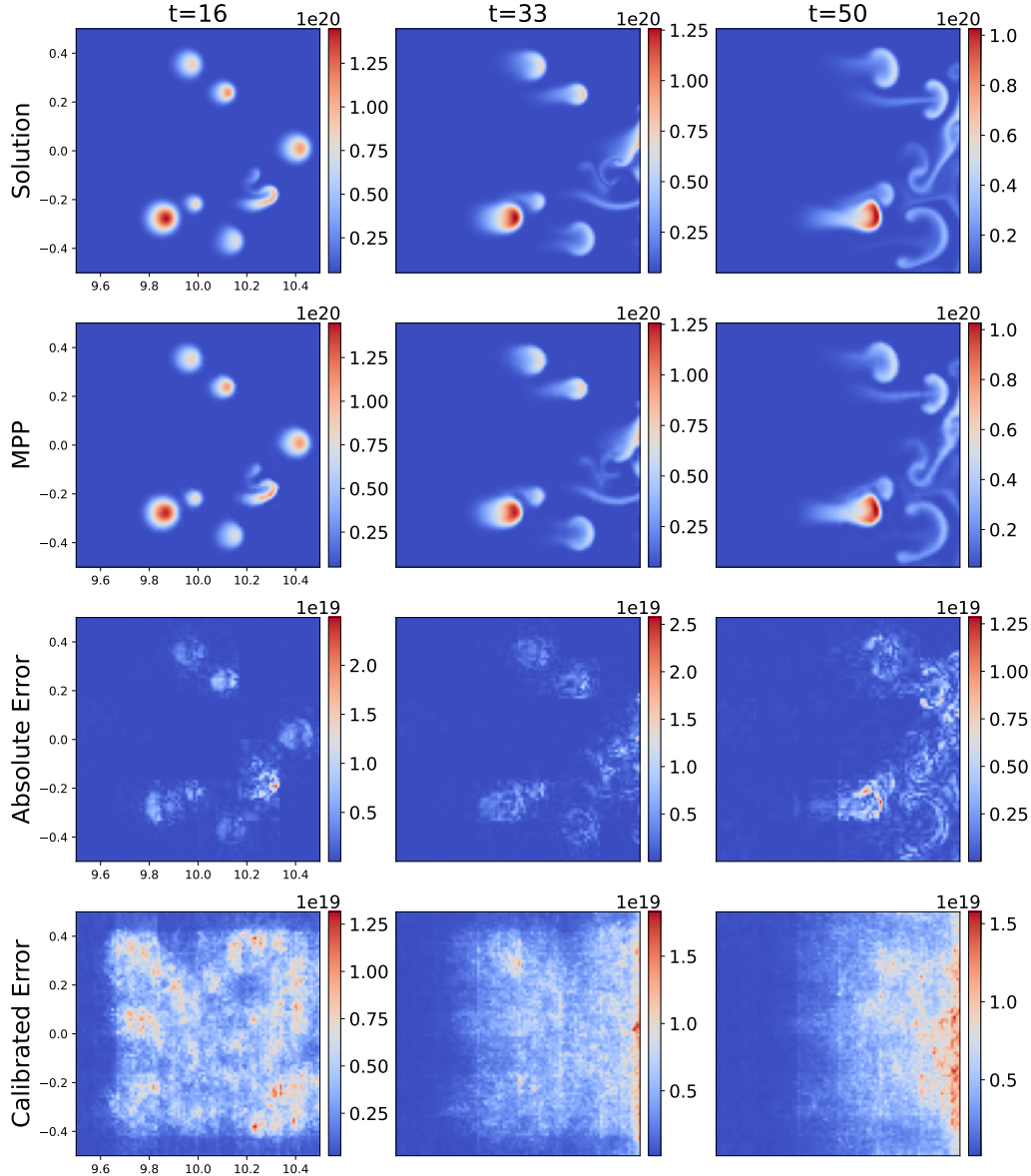


Figure 12: Demonstrating the Performance of the Fine-tuned MPP model in capturing the MHD behaviour. The top row demonstrates the numerical solution, the second row shows the model output, the third row shows the absolute error and the bottom row demonstrates the calibrated error providing 95% coverage. Being a deterministic model, the calibration procedure results in generating general uncertainties for regions of major dynamics within the dataset, not specific to the prediction instance.

forecasting models. Traditional weather forecasting models typically combine PDEs describing large-scale interactions and parametrizations describing subgrid-scale physical processes (Kalnay, 2002). Data-driven machine learning models approximate this whole process with a single neural network model. This allows for orders of magnitude faster forecasting speed and, when training on data incorporating observations, also more accurate forecasts (Bouallègue et al., 2024; Bi et al., 2023; Kurth et al., 2023; Lam et al., 2023).

Due to the chaotic nature of the weather system, capturing uncertainty in weather forecasts has long been an important consideration both in research and operations. Such probabilistic modeling has typically been achieved by ensemble forecasting, where perturbations are used to produce samples of possible forecast trajectories (Coiffier, 2011). Existing data-driven models are still largely deterministic (Rasp et al., 2024). There are attempts to produce ensemble forecasts using machine learning models by perturbing initial states (Kurth et al., 2023; Chen et al., 2023b), training multiple models (Graubner et al., 2022) or generative modeling (Hu et al., 2023; Price et al., 2023; Oskarsson et al., 2024). Fundamentally, ensemble forecasting always requires a computational cost proportional to the number of ensemble members i.e. the number of forecasts made via perturbations. In contrast, CP offers a cheap method to immediately quantify forecast uncertainty for a time, position, and variable of interest. This uncertainty can be used by meteorologists interpreting the forecast, conveyed to decision-makers reacting to extreme weather events or directly presented to end-user looking up the forecast for the coming week. As CP enables UQ for one single forecast output by the model, it is directly applicable to existing deterministic machine learning models. A limitation of scalar uncertainty estimates is that there are no samples of the distribution over the atmospheric state. In some scenarios it can be valuable to inspect such samples to gain an understanding of how different weather scenarios are unfolding.

3.7.1 MODEL

We apply CP to the Graph-FM model of Oskarsson et al. (2024). Graph-FM is a graph-based neural weather prediction model (Keisler, 2022; Lam et al., 2023), where a hierarchical Graph Neural Network (GNN) is utilized for producing the forecast. Let X^t denote the full weather state at time step t , including multiple atmospheric variables modeled for all grid cells in some discretization. Examples of such atmospheric variables are temperature, wind, geopotential and solar radiation. The GNN g in Graph-FM represents the single time step prediction

$$X^{t+1} = g(X^{t-1:t}, F^{t+1}) \quad (5)$$

where F^{t+1} are known forcing inputs that should not be predicted. Taking the two past states as inputs to g allows the model to make use of both magnitude and first derivative information. Equation (5) can be applied iteratively to roll out a complete forecast of T time steps. The full forecasting model can thus be viewed as mapping from initial weather states $X^{-1:0}$ and forcing $F^{1:T}$ to a forecast $X^{1:T}$. The forecast $X^{1:T}$ is a tensor of shape $T \times N_x \times N_y \times N_{\text{var}}$, where N_{var} is the number of atmospheric variables modeled. We consider two versions of Graph-FM, trained with different loss functions:

- **Graph-FM (MSE):** Graph-FM trained with a weighted MSE loss. This model outputs only a single prediction, to be interpreted as the mean of the weather state.

- **Graph-FM (NLL):** A version of Graph-FM that outputs both the mean and standard deviation for each time, variable and grid cell. This model was trained with a Negative Log-Likelihood (NLL) loss, assuming a diagonal Gaussian predictive distribution (also referred to as the uncertainty loss (Chen et al., 2023a)). Apart from the change of loss function the training setup was identical.

For the Graph-FM (MSE) we compute non-conformity scores using the RES strategy. As the Graph-FM (NLL) is probabilistic, we there use STD non-conformity scores. Note that these are computed based on the standard-deviations directly output from the model, rather than from sample-estimates based on MC dropout.

3.7.2 LIMITED AREA FORECASTING

In this first experiment we apply CP to a limited area version of Graph-FM. Forecasts are here produced for a limited area covering the Nordic region. These Graph-FM models were trained on the limited area dataset from Oskarsson et al. (2024), consisting of forecasts from the MEPS system (Müller et al., 2017). One such forecast includes $N_{\text{var.}} = 17$ variables modeled on a $N_x \times N_y = 238 \times 268$ grid over $T = 19 \times 3h$ time steps (up to 57 hour lead time). When Graph-FM is used in a limited area configuration, it produces weather forecasts for a specific sub-area of the globe. To achieve this, boundary conditions along the edges of the forecasting area are given as important forcing inputs. The exact models used have 4 graph processing layers and use 64-dimensional latent representations. We refer to Oskarsson et al. (2024) for further details about the model and data.

We use forecasts started during September 2021³ as our calibration data set and forecasts started during September 2022 as test data. By using the same month for calibration and testing we minimize the effect of distributional shifts due to seasonal effects. Having access to calibration data from the same month, collected the previous year, is a reasonable assumption in practical settings.

Figure 13 shows the ground truth, predicted forecast and the conformalised error intervals for temperature 2m above ground. Considering the autoregressive nature of Graph-FM, the error accumulates and grows further in time, which is accurately captured by the CP framework (refer Figure 16).

Figure 14 shows the empirical coverage for the test set. With CP we can achieve calibrated uncertainty estimates for both versions of Graph-FM. Of great interest in the weather forecasting setting is the uncertainty for specific future time points. We visualise this by plotting the width of the error bars for all spatial locations at different lead times in an example forecast. Such plots for shortwave solar radiation are shown in Figure 15 and for geopotential in Figure 16.

Figure 15 highlights an important difference between the two methods for computing non-conformity scores. As the shortwave solar radiation is close to 0 during the night, it is easy for the model to predict. During the day this is far more challenging. With the RES non-conformity scores, used for Graph-FM (MSE) in Figure 15a, the width of the

3. For calibration we specifically use forecasts started during the dates 2021-09-04 – 2021-09-30. The model was trained on forecasts started during the last days of August, which are rolled out over the first days of September. To avoid strong correlations to the training data we use only forecasts from September 4 onwards for calibration.

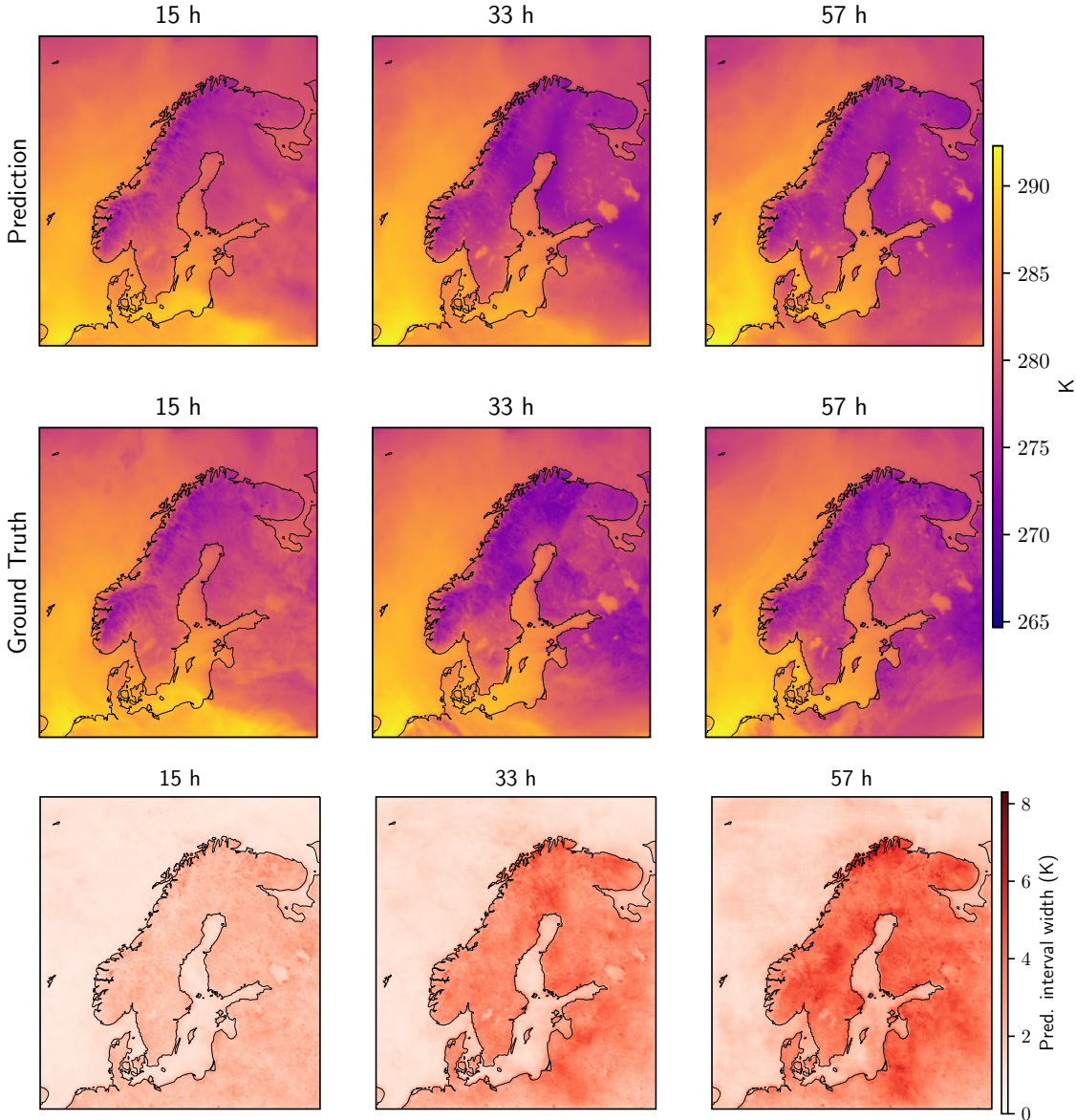


Figure 13: Prediction (top), Ground Truth (middle) and width of the error bars (bottom) at $\alpha = 0.05$ for predicting the temperature 2m above ground ($2t$) using Graph-FM (MSE).

predictive intervals are determined during calibration, and does not change depending on the forecast from the model. As a specific lead time can fall both during day and night, depending on the initialization time, CP will give large error bars also during the night. This can be compared to the results for Graph-FM (NLL) in Figure 15b, using STD non-conformity scores. In this case the bounds are very tight for lead times during the night (33 h and 57 h). It can also be noted that for Graph-FM (NLL) at lead time 15 we see clear spatial features appearing in the error bars themselves. This corresponds to higher forecast

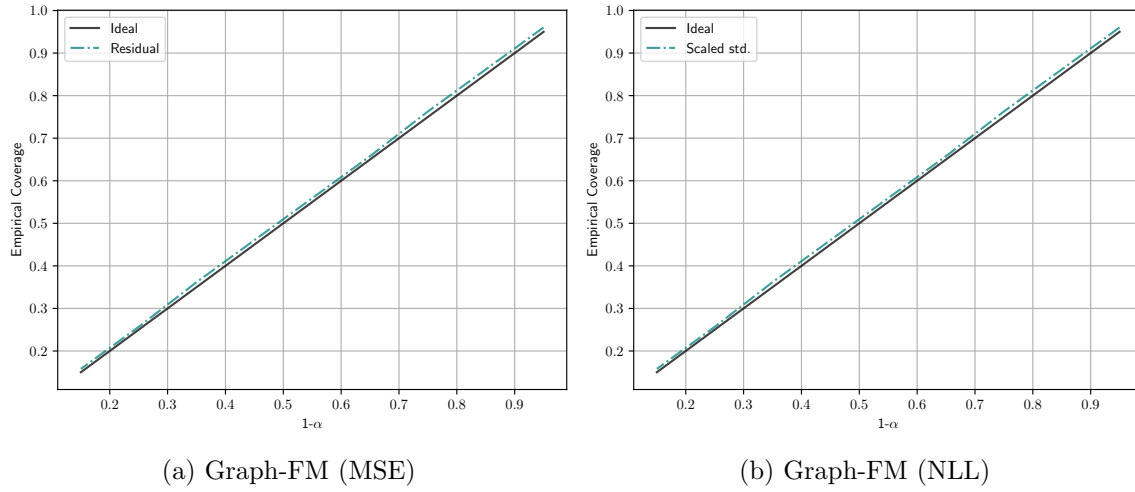


Figure 14: Empirical Coverage for weather forecasting models.

uncertainty in areas of rapid change. The forecast-dependent patterns for Graph-FM (NLL) thus have desirable properties, but this relies on having a model that outputs (potentially uncalibrated) standard-deviations.

3.7.3 GLOBAL FORECASTING

We next experiment with CP for global weather forecasting. The models used are again Graph-FM (MSE) and Graph-FM (NLL), but here applied on the full globe. These models are trained on a version of the ERA5 reanalysis dataset (Hersbach et al., 2020) using a 1.5° latitude-longitude grid. The global models have 8 graph processing layers and use 256-dimensional latent representations. Each forecast includes 5 surface variables and 6 atmospheric variables, each modeled at 13 different vertical pressure levels in the atmosphere. Due to the large number of variables forecast (83 in total) we here only perform CP for a subset of these. This subset includes all surface variables and the atmospheric variables at pressure level 700 hPa. This results in a total of $N_{\text{var.}} = 11$ variables, modeled on a $N_x \times N_y = 240 \times 121$ grid over $T = 40$ time steps (up to 10 days lead time with 6 h time steps). We note that a strength of the CP framework is that uncertainty quantification can be performed per variable, alleviating memory issues during calibration. Because of this the procedure could trivially be extended to the full set of variables, as long as the full forecasts are stored. We again refer to Oskarsson et al. (2024) for more details about the global models and data configuration.

For the global experiment we use full years of forecasts for calibration and evaluation, all started from ERA5 as initial conditions. Forecasts at 00 and 12 UTC each day of 2018 are used as the calibration set and a similar set of forecasts for 2019 used as test set⁴. The ground truth is given by ERA5 at each forecasted time point. Using a full year for calibration allows for capturing the model performance across all different seasons. This

4. We remove forecasts started during the last 10 days of 2018 from the calibration set to avoid strong correlations with the test data at the start of 2019. Note that forecasts in the test set started during the last days of 2019 will extend into time points in 2020.

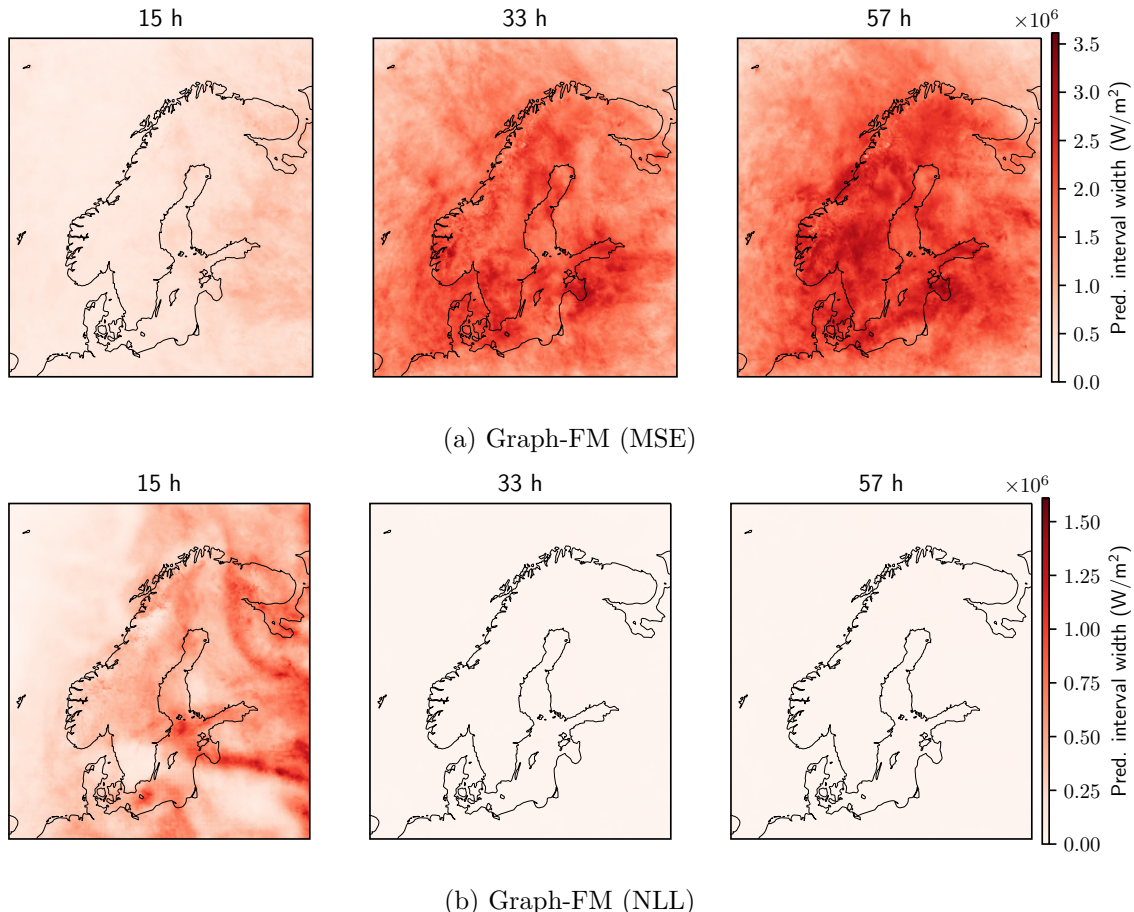


Figure 15: Width of predictive interval at $\alpha = 0.05$ for shortwave solar radiation (`nswrs`) in an example forecasts. Note that for Graph-FM (MSE) these widths are constant after calibration, while for Graph-FM (NLL) they depend on the predicted standard deviations for the specific forecast. This is most noticeable by Graph-FM (NLL) having very tight bounds during the night (lead times 33 h and 57 h), when the short wave solar radiation is close to 0 and easy to predict.

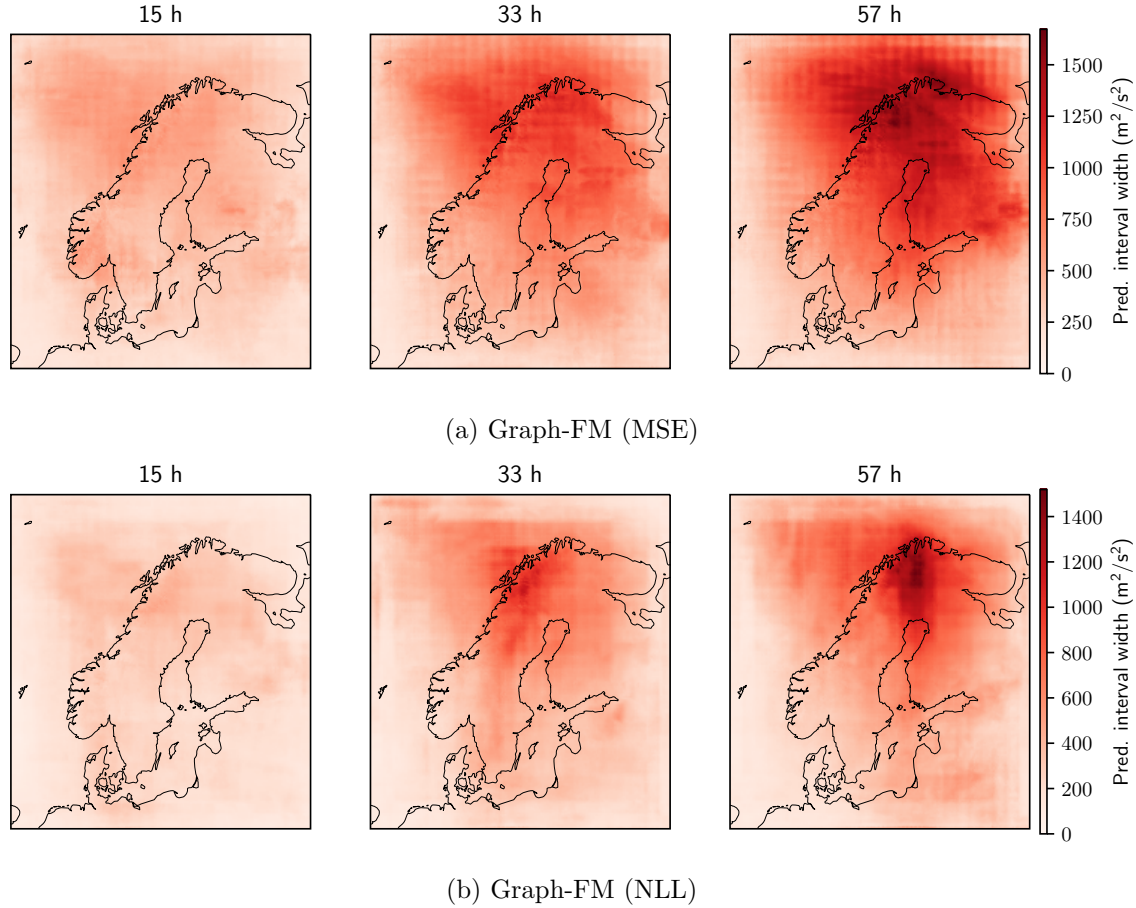


Figure 16: Width of predictive interval at $\alpha = 0.05$ for geopotential at 500 hPa (z500). Both models show a certain spatial pattern, especially for longer lead times. This pattern can be connected to how the GNN in Graph-FM is defined over the forecasting area.

allows for calibrating the model once, and then using the computed \hat{q} values for the full next year of forecasts. However, any distributional shift due to climate variations from one year to the next remain. We note that in practice this does not seem to cause any major issue for achieving the desired coverage.

Figure 17 shows an example prediction from Graph-FM (MSE) and corresponding error bars. Global forecasting up to 10 days is a more challenging task than the limited area modeling up to 57 h. We see that at 10 days the model prediction fails to capture much of the patterns in the ground truth data. Importantly, this is accurately captured in the error bars, which increase with the lead time to high values at 10 days.

In Figures 18 and 19 we plot the width of the error bar for specific humidity and wind. Similar to the limited area case, we note for Graph-FM (NLL) the error bars corresponds to patterns in the forecast itself, due to the use of predicted standard deviations from the model. For Graph-FM (MSE) the plots instead highlight the regions where predictions are more challenging in general, across all forecasts. Additional plots from the weather forecasting experiments are given in Appendix H.

As for all experiments, we include results for the weather forecasting models in Table 1. In both the global and limited area setting CP successfully produces calibrated error bars. For the Graph-FM (NLL) model the original standard deviations output by the model are too low, leading to invalid error bars and insufficient coverage. After applying CP however the error bars are nicely calibrated. We generally see that the Graph-FM (NLL) has tighter error bars than Graph-FM (MSE). This can be attributed to these being input-dependent, specific to each forecast from the model.

3.7.4 DISCUSSION ON EXCHANGEABILITY

Traditionally the CP framework is limited in application to time-series modelling as it fails the exchangeability assumption. Previous research has looked into fixing this violation of exchangeability by accounting for the distribution shift using weighted conformal techniques (Tibshirani et al., 2019), but becomes limited in application in multi-variate settings. Other work has explored CP for multi-variate time series forecasting, where each time-series is treated as an exchangeable observation (Stankeviciute et al., 2021). Within the weather modelling tasks outlined in this section, we maintain exchangeability by treating each modelling task as an Initial Boundary Value Problem (IBVP, boundary given by the forcing terms in Equation (5)). As given in Equation (5), the model takes in the initial conditions, $\mathcal{X} \in \mathbb{R}^{T_{in=1} \times N_x \times N_y \times N_{var}}$ and is auto-regressively rolled out T_{out} steps to obtain the output $\mathcal{Y} \in \mathbb{R}^{T_{out} \times N_x \times N_y \times N_{var}}$. Being dependent on the initial conditions alone and being rolled out for a fixed number of steps, each input-output pair as mathematically outlined in Section 2.1.2 and visually represented in Figure 20 can be treated as an exchangeable pair. We are allowed to make this assumption on exchangeability since the model is agnostic to the temporal nature of the dataset beyond the autoregressive roll-out of each forward prediction, typical of an initial boundary value problem i.e. the neural weather forecast starting from 18:00 3rd January is independent of the forecast made using the neural weather models starting at 12:00 1st January. Here the calibration dataset is seen as samples from an extremely large distribution which effectively characterises the entirety of the entire month/year under consideration. Thus, by combining our preservation

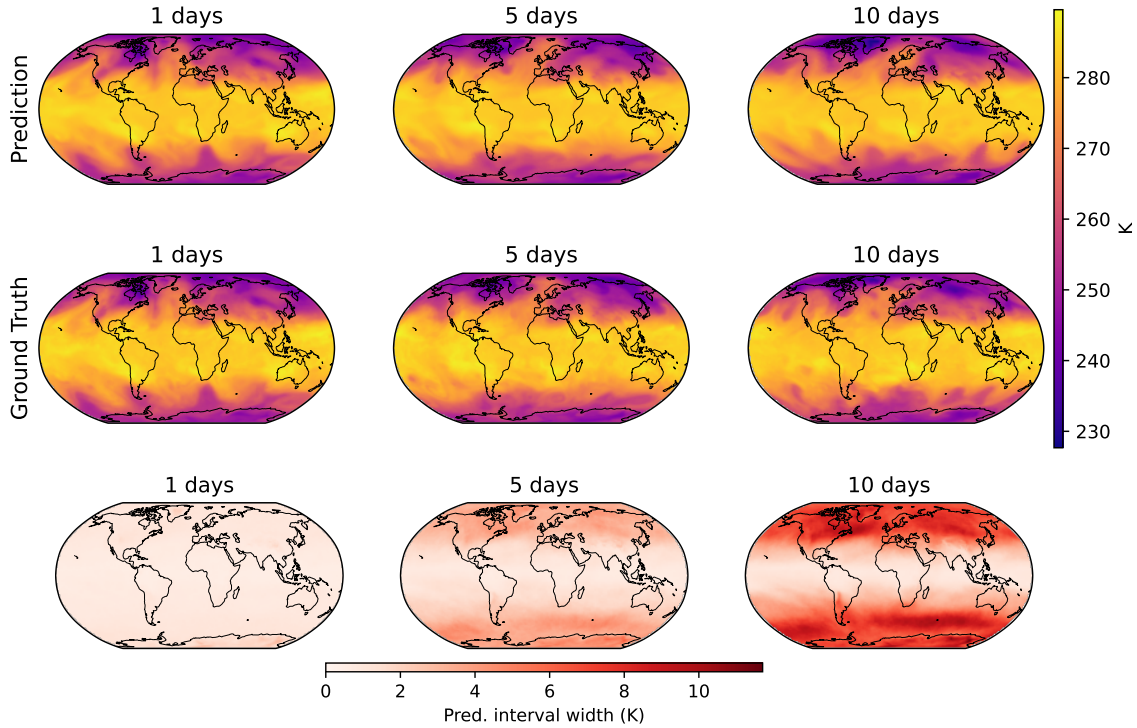


Figure 17: Prediction (top), Ground Truth (middle) and width of the error bars (bottom) at $\alpha = 0.15$ for predicting the temperature at 700 hPa ($t700$) using Graph-FM (MSE).

of spatio-temporal structure as outlined in Section 2.1.2 and by treating the neural weather models as initial boundary value problems, we are able to maintain exchangeability across the calibration datasets, allowing us to perform CP.

Though the above description discusses about exchangeability across the calibration dataset, it does not extend across to the prediction set. For each of the experiments within the limited area and global weather forecasting, we make the assumption that the climate does not vary significantly across the years under consideration for the calibration and prediction sets.

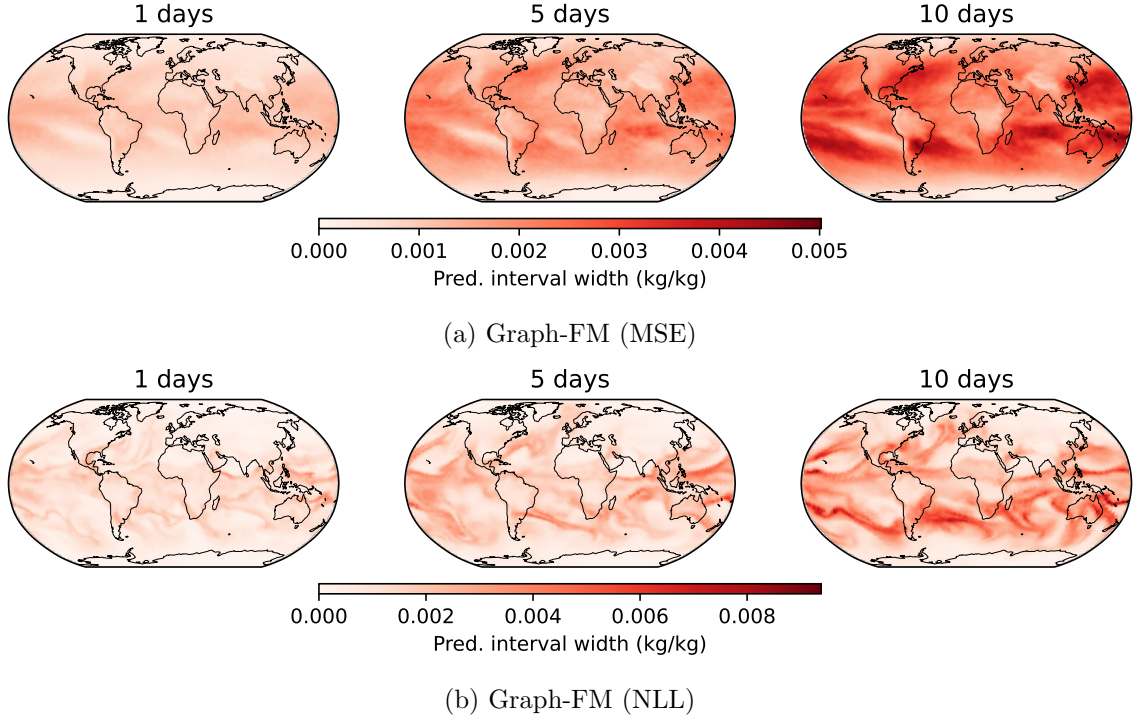


Figure 18: Width of predictive interval at $\alpha = 0.15$ for specific humidity at 700 hPa (q700).

3.8 Camera Diagnostic on a Tokamak

The Mega-Ampere Spherical Tokamak (MAST) is an experimental fusion device at the UK Atomic Energy Authority. It was equipped with fast camera imaging diagnostics at several points across the Tokamak for capturing images within the visible spectrum, capturing the plasma evolution in real-time⁵. These Photron cameras⁶ are essential diagnostics that contributed to fundamental understandings of key plasma phenomena in Tokamaks in recent years (Kirk et al., 2006). While camera data have mostly been used for qualitative analysis, recently it have been exploited to provide statistical insight into plasma turbulence (Walkden et al., 2022), as well as global instabilities (disruptions) (Ham et al., 2022).

In our previous work (Gopakumar et al., 2024), we demonstrated the utility of the FNO to forecast the evolution of the plasma within the Tokamak. Within that work, the FNO was trained to take in an input sequence of 10 camera frames and predict a sequence of the next 10 camera frames of the plasma within the Tokamak. The model is trained on sequences of frames characterising the entire duration of a plasma shot within the MAST Tokamak. In this work, we apply the CP framework across the FNO-camera using the AER nonconformity score to provide valid error bars to the plasma evolution forecasts. For results and further information about the camera data, FNO and the training setup used, we advise the reader to refer to the original work by (Gopakumar et al., 2024).

5. <https://ccfe.ukaea.uk/research/mast-upgrade/>

6. <https://photon.com/>

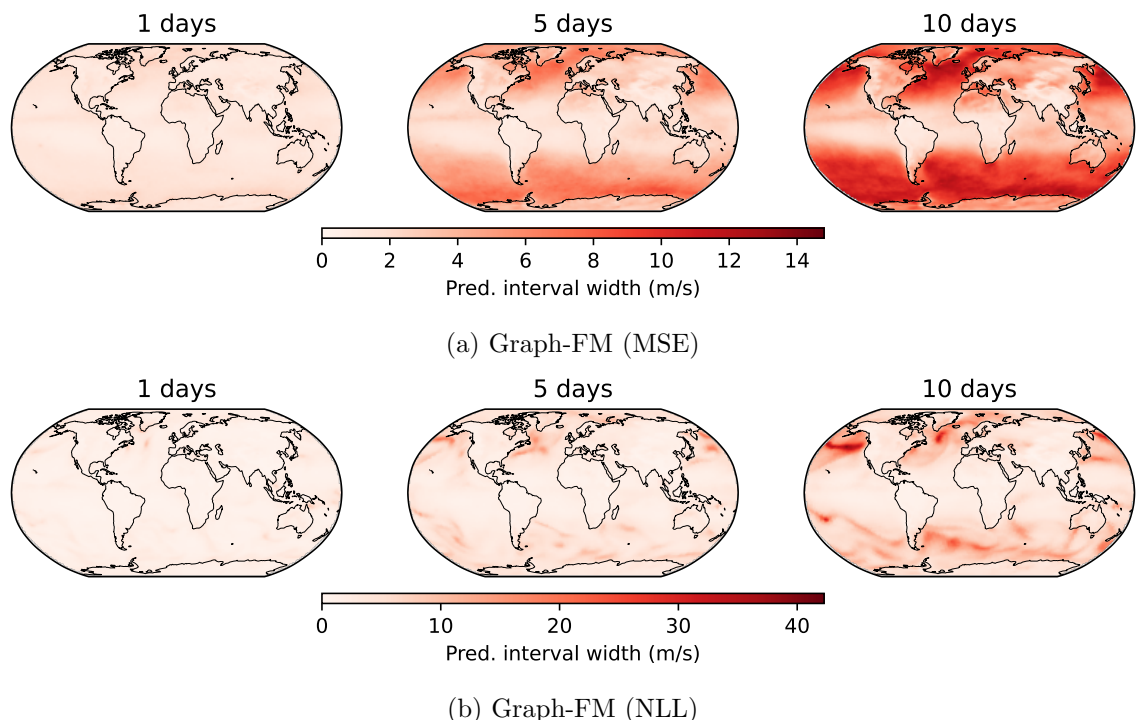


Figure 19: Width of predictive interval at $\alpha = 0.15$ for u -component of wind at 10 m above ground (10u).

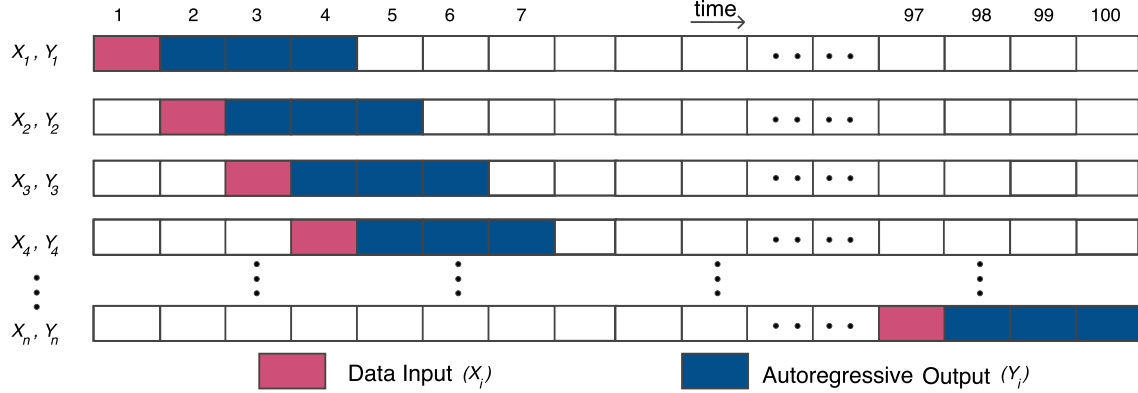


Figure 20: Constructing exchangeable input-output pairs from a time series dataset. Calibration dataset is arbitrarily characterised by a spatio-temporal dataset spanning 100 time instances, where the model takes in the field at a day and autoregressively predicts for the next 3 time instances. Since the model represents an initial boundary value problem, we are able to break each input-output (X_i, Y_i) as an exchangeable data point, essentially sampled from a distribution spanning the entire month.

Though the FNO is trained to predict the evolution of plasma for the entire time duration of a plasma shot, similar to Section 3.7, the modelling task and the data are structured to represent that of an initial value problem. As represented in Figure 20, the model takes in a fixed time sequence and outputs a fixed time sequence, its output is fully determined by the initial sequence of frames provided to the model. In our framework, we apply CP across the entire spatio-temporal domain of the output simultaneously and not sequentially, where the temporal nature of the output (the 10 time frames) is kept intact. Figure 22 visualises the error bars obtained using the CP framework over the FNO used to forecast the plasma evolution across the central solenoid of the Tokamak and obtains exact coverage as indicated in Appendix I.

We have the following arguments to support the validity of using CP for this time dependant problem, 1) only the calibration dataset and the prediction X_{n+1} are required to be exchangeable, 2) we predict errors over an entire time interval simultaneously, not sequentially, and 3) we assume there is no large shift in the data between the calibration shot and prediction shot. The exchangeability requirement across the calibration and prediction shot requires them to follow similar plasma discharge profiles and device conditions. Predicting across a characteristically different shot violates this assumption and suffers from lack of coverage as shown in Figure 21.

4 Discussion

4.1 Strengths

In physical modelling and engineering design, ML models are deployed as emulators to replace expensive simulation codes and control algorithms, so that they can help efficiently and inexpensively perform design optimisation and uncertainty quantification (i.e., evaluating

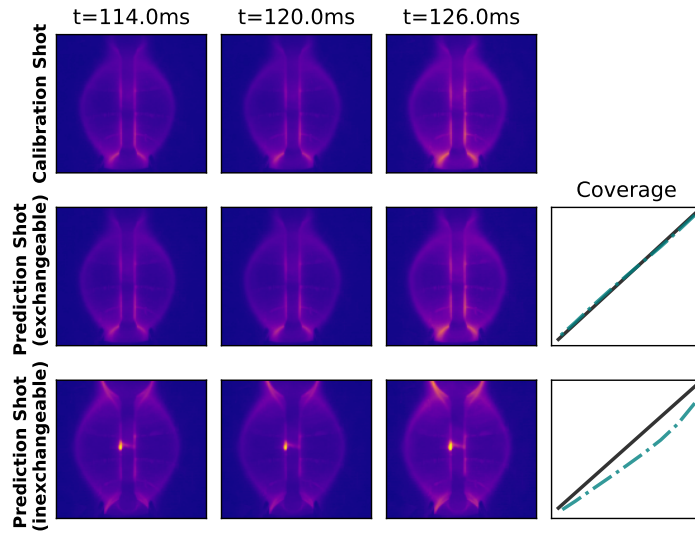


Figure 21: Comparing coverage obtained across prediction shots that are exchangeable (similar plasma profiles) to the calibration shot and that is in-exchangeable (dissimilar plasma profiles).

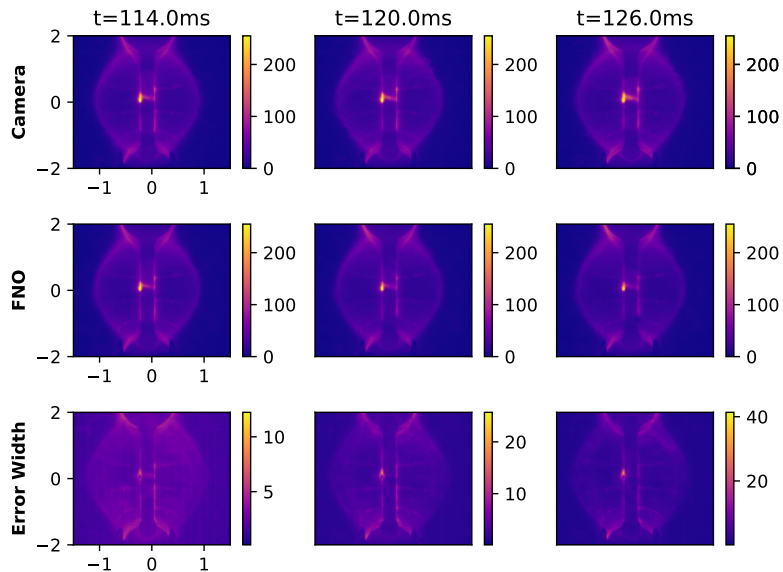


Figure 22: Camera (top), FNO (middle) and the prediction interval width obtained using CP with $\alpha = 0.5$ (bottom).

input data uncertainty and computing risks of undesirable scenarios). For these applications, ideally, the surrogate is trained once for simulation data and then deployed for a particular application with few options for further data acquisition and fine-tuning. However, in these cases, it is important to equip predictions with credible uncertainty estimates as more physics-based surrogate models evolve from a research environment to a production suite. In such critical modelling tasks, the validity of uncertainty plays a crucial role in determining the efficacy of a model (Begoli et al., 2019). Conformal prediction is suitable for these settings as it provides statistical guarantees for the coverage established by the framework. Aside from validity in coverage, CP provides the added benefit of application across pre-trained models, without requiring any knowledge about the model architecture (also not needing any architectural modifications) and its training regime. Within this paper, we showed that the CP framework can be formalised and set to obtain statistically valid marginal coverage over high-dimensional spatio-temporal outputs, beating the curse of dimensionality with near-zero computational costs. It provides statistical guarantees over the coverage of the prediction datasets while being relatively inexpensive and trivial in its implementation. CP also provides a methodology for uncertainty quantification that allows further testing of the model’s *usefulness* in a particular prediction regime.

4.2 Limitations

Many AI applications in scientific domains employ machine learning models that are trained and deployed without considering specific application contexts. These ML workflows often have constraints on retraining capabilities or obtaining additional data from simulations. The following paragraphs will explore potential limitations of this approach and discuss various solutions proposed in the literature.

Marginal coverage. The main prohibitive assumption is the fact the coverage guarantees (1) only provide *marginal coverage*, i.e., coverage is only valid for predictions averaged over all labels. For surrogacy, *conditional coverage* is desirable

$$\mathbb{P}(Y_{n+1} \in \mathbb{C}^\alpha | X_{n+1}) \geq 1 - \alpha, \quad (6)$$

i.e., to wish for \mathbb{C}^α to be valid for each specific label the model predicts. An ideal framework would maintain coverage on each particular prediction, and not averaged over a dataset. Although this feature is not possible to guarantee in general, it can be approximated reasonably well (Vovk, 2012).

Within the formulation considered in this paper, it must be reiterated that the coverage is estimated and hence, guaranteed cell-wise across the predicted spatio-temporal tensor. It does not guarantee a joint coverage that extends across the full scale of the bounds of the interested prediction domain. Though there has been work done in extending from marginal coverage across each cell to joint coverage across each domain, they fail to scale with dimensionality (Diquigiovanni et al., 2021; Messoudi et al., 2021, 2022).

An alternative solution without re-evaluating a novel calibration dataset is to use covariate shifting (Tibshirani et al., 2019). An additional assumption is however required: both the probability density of the training calibration distribution and of the new distribution must be known or could be inferred effectively. This is a fairly weak assumption in surrogate modelling, where the training calibration distribution is certainly known (the

distribution we originally trained our surrogate on), and the new distribution’s density could perhaps be estimated if only sample data is obtained. Probability density estimation required for performing CP under covariate shift fails to scale effectively with high dimensionality (Quionero-Candela et al., 2009).

Data Intensive. Though the framework does not require any retraining, it still requires additional simulation / experimental data to perform the calibration, which might be prohibitively expensive. The statistical coverage guarantees from the CP framework itself lie on a beta distribution as given in Equation (4), governed by the number of calibration data points. We further conduct an empirical study of the impact of calibration data on the obtained coverage which is provided in Appendix G.

No predictive distribution. Unlike Bayesian methods, which provide probability distribution as predictions, conformal prediction provides prediction *sets*. Distributions are simpler to compute with, as they may be simply evaluated or propagated by Monte Carlo sampling. They also provide precise probabilities for events or any derived risk calculation. Methods of performing calculations such as calibration, propagation, or computing probabilities of events with prediction sets are not obvious, which is perhaps a reason why frequentist methods are not as widely used in UQ for scientific applications.

Recently, however, Cella and Martin (2022) have proposed an imprecise probabilistic interpretation of conformal prediction, and describe how probability measures may be bounded in conformalised regression and classification problems. They describe how the contour function of a plausibility measure (i.e., a possibility measure) can be computed from the conformal prediction sets. This could allow for the uncertainty estimates from conformal prediction to be further propagated and evaluated (Balch, 2012; Hose and Hanss, 2021), and makes a wider range of uncertainty quantification tasks accessible to confidence-based methods like conformal prediction.

Although Bayesian posteriors are perhaps also more informative, Balch et al. (2019), they must be treated with caution for modelling epistemic uncertainty. Martin (2019) describes this in a mathematically rigorous way, through the false-confidence theorem, stating that any additive model of uncertainty (e.g., a precise probability) is not guaranteed to provide correct inferences on all hypotheses: that there are certain events that a posterior distribution will assign a high probability to when the true probability is low. Although predictive distributions are simpler to understand and work with, their use does not come without its challenges.

Input Independence. Uncertainty ($\sim \hat{q}$) is added to the model outputs as prediction sets are independent of the model inputs and a function of the calibration dataset. In more Bayesian methods, the prediction uncertainty, estimated in the posterior is seen as a function of the prior and the likelihood, hence varying for each region of the prediction regime. Within the deterministic models explored within this work (using nonconformity score AER), the value of the error ($\sim \hat{q}$) is determined before the model prediction and remains fixed across the inference regime. This is exceptionally clear in the case of the fine-tuned foundation physics model (see Figure 12, where the error bars indicate the global error approximation and not on a case-by-case basis. For probabilistic models (using STD nonconformity score) this is less severe as the error bar is not just a function of \hat{q} but also of the standard deviation output from the model. This allows for the prediction sets to be more flexible and adjust as a function of the model inputs (see Figure 2). Though there has been

work on making the CP framework further input dependent (Johansson et al., 2021), they still require augmenting deterministic models through ensembles or architectural changes.

5 Conclusion

In this paper, it is shown that by maintaining the exchangeability of the data across the spatio-temporal domain (i.e. by preserving the tensorial shape), conformal prediction provides valid error bars (i.e., satisfied Equation (1)) to expensive surrogate models for scientific applications, even if they make out-of-distribution predictions. Our empirical studies demonstrate that conformal prediction can be applied to any pre-trained / fine-tuned model for obtaining statistically guaranteed coverage, irrespective of the model configuration, training conditions and dimensionality of the outputs. One of the crucial highlights of the study is that CP can help provide guaranteed prediction sets across a new set of PDE solutions (out-of-distribution data), different to that which the model was conditioned on. Our work benchmarks against three kinds of calibration methods (nonconformity scores), across deterministic and probabilistic models, ensuring validity for the coverage. Although we focus on providing guaranteed coverage for modelling spatio-temporal data, we believe that our findings extend to any models predicting outputs with fixed tensorial output shapes and with exchangeable calibration and prediction regimes.

The code used for the study can be found in <https://github.com/gitvicky/Spatio-Temporal-UQ>

6 Acknowledgements

The authors would like to thank Anima Anandkumar and Zongyi Li from Caltech for their help with defining neural operators and extending them to complex physics cases. The authors would also like to thank Michael McCabe at the Flatiron Institute for his help in setting up the Multi-Physics Pretrained foundation physics model and extending it to a Fusion-relevant database. This research was supported by the Excellence Center at Linköping–Lund in Information Technology (ELLIIT). Our computations were enabled by the Berzelius resource at the National Supercomputer Centre, provided by the Knut and Alice Wallenberg Foundation.

References

M. Abdar, F. Pourpanah, S. Hussain, D. Rezazadegan, L. Liu, M. Ghavamzadeh, P. Fieguth, X. Cao, A. Khosravi, U. R. Acharya, V. Makarenkov, and S. Nahavandi. A review of uncertainty quantification in deep learning: Techniques, applications and challenges. *Information Fusion*, 76:243–297, 2021. ISSN 1566-2535. doi: <https://doi.org/10.1016/j.inffus.2021.05.008>. URL <https://www.sciencedirect.com/science/article/pii/S1566253521001081>.

M. S. Alhajeri, F. Abdullah, Z. Wu, and P. D. Christofides. Physics-informed machine learning modeling for predictive control using noisy data. *Chemical Engineering Research and Design*, 186:34–49, 2022. ISSN 0263-8762. doi: <https://doi.org/10.1016/j.cherd.2022.07.035>. URL <https://www.sciencedirect.com/science/article/pii/S0263876222003847>.

B. Alkin, A. Fürst, S. Schmid, L. Gruber, M. Holzleitner, and J. Brandstetter. Universal physics transformers: A framework for efficiently scaling neural operators, 2024.

A. N. Angelopoulos and S. Bates. Conformal prediction: A gentle introduction. *Found. Trends Mach. Learn.*, 16(4):494–591, mar 2023. ISSN 1935-8237. doi: 10.1561/2200000101. URL <https://doi.org/10.1561/2200000101>.

K. Azizzadenesheli, N. Kovachki, Z. Li, M. Liu-Schiavini, J. Kossaifi, and A. Anandkumar. Neural operators for accelerating scientific simulations and design. *Nature Reviews Physics*, 04 2024. ISSN 2522-5820. doi: 10.1038/s42254-024-00712-5. URL <https://doi.org/10.1038/s42254-024-00712-5>.

M. S. Balch. Mathematical foundations for a theory of confidence structures. *International Journal of Approximate Reasoning*, 53(7):1003–1019, 2012.

M. S. Balch, R. Martin, and S. Ferson. Satellite conjunction analysis and the false confidence theorem. *Proceedings of the Royal Society A*, 475(2227):20180565, 2019.

P. Baldi, K. Cranmer, T. Faucett, P. Sadowski, and D. Whiteson. Parameterized neural networks for high-energy physics. *The European Physical Journal C*, 76(5):235, 04 2016. ISSN 1434-6052. doi: 10.1140/epjc/s10052-016-4099-4. URL <https://doi.org/10.1140/epjc/s10052-016-4099-4>.

E. Begoli, T. Bhattacharya, and D. Kusnezov. The need for uncertainty quantification in machine-assisted medical decision making. *Nature Machine Intelligence*, 1(1):20–23, 1 2019. ISSN 2522-5839. doi: 10.1038/s42256-018-0004-1. URL <https://doi.org/10.1038/s42256-018-0004-1>.

P. M. Bellan. *Fundamentals of Plasma Physics*. Cambridge University Press, 2006. ISBN 9780511562105. URL <https://books.google.co.uk/books?id=CoPtzQEACAAJ>.

G. Bertone, M. P. Deisenroth, J. S. Kim, S. Liem, R. Ruiz de Austri, and M. Welling. Accelerating the bsm interpretation of lhc data with machine learning. *Physics of the Dark Universe*, 24:100293, 2019.

K. Bi, L. Xie, H. Zhang, X. Chen, X. Gu, and Q. Tian. Accurate medium-range global weather forecasting with 3d neural networks. *Nature*, pages 1–6, 2023.

R. Bommasani, D. A. Hudson, E. Adeli, R. Altman, S. Arora, S. von Arx, M. S. Bernstein, J. Bohg, A. Bosselut, E. Brunskill, E. Brynjolfsson, S. Buch, D. Card, R. Castellon, N. Chatterji, A. Chen, K. Creel, J. Q. Davis, D. Demszky, C. Donahue, M. Doumbouya, E. Durmus, S. Ermon, J. Etchemendy, K. Ethayarajh, L. Fei-Fei, C. Finn, T. Gale, L. Gillespie, K. Goel, N. Goodman, S. Grossman, N. Guha, T. Hashimoto, P. Henderson, J. Hewitt, D. E. Ho, J. Hong, K. Hsu, J. Huang, T. Icard, S. Jain, D. Jurafsky, P. Kalluri, S. Karamcheti, G. Keeling, F. Khani, O. Khattab, P. W. Koh, M. Krass, R. Krishna, R. Kuditipudi, A. Kumar, F. Ladhak, M. Lee, T. Lee, J. Leskovec, I. Levent, X. L. Li, X. Li, T. Ma, A. Malik, C. D. Manning, S. Mirchandani, E. Mitchell, Z. Munyikwa, S. Nair, A. Narayan, D. Narayanan, B. Newman, A. Nie, J. C. Niebles, H. Nilforoshan, J. Nyarko, G. Ogut, L. Orr, I. Papadimitriou, J. S. Park, C. Piech, E. Portelance, C. Potts, A. Raghunathan, R. Reich, H. Ren, F. Rong, Y. Roohani, C. Ruiz, J. Ryan, C. Ré, D. Sadigh, S. Sagawa, K. Santhanam, A. Shih, K. Srinivasan, A. Tamkin, R. Taori, A. W. Thomas, F. Tramèr, R. E. Wang, W. Wang, B. Wu, J. Wu, Y. Wu, S. M. Xie, M. Yasunaga, J. You, M. Zaharia, M. Zhang, T. Zhang, X. Zhang, Y. Zhang, L. Zheng, K. Zhou, and P. Liang. On the opportunities and risks of foundation models, 2022.

Z. B. Bouallègue, M. C. A. Clare, L. Magnusson, E. Gascón, M. Maier-Gerber, M. Janoušek, M. Rodwell, F. Pinault, J. S. Dramsch, S. T. K. Lang, B. Raoult, F. Rabier, M. Chevallier, I. Sandu, P. Dueben, M. Chantry, and F. Pappenberger. The rise of data-driven weather forecasting: A first statistical assessment of machine learning-based weather forecasts in an operational-like context. *Bulletin of the American Meteorological Society*, 105(6):E864 – E883, 2024. doi: 10.1175/BAMS-D-23-0162.1. URL <https://journals.ametsoc.org/view/journals/bams/105/6/BAMS-D-23-0162.1.xml>.

J. Brandstetter, D. E. Worrall, and M. Welling. Message passing neural PDE solvers. In *International Conference on Learning Representations*, 2022. URL <https://openreview.net/forum?id=vSix3HPYKSU>.

N. Carey, L. Zanisi, S. Pamela, V. Gopakumar, J. Omotani, J. Buchanan, and J. Brandstetter. Data efficiency and long term prediction capabilities for neural operator surrogate models of core and edge plasma codes, 2024. URL <https://arxiv.org/abs/2402.08561>.

L. Cella and R. Martin. Validity, consonant plausibility measures, and conformal prediction. *International Journal of Approximate Reasoning*, 141:110–130, 2022.

S. Chandrasekhar. Stochastic problems in physics and astronomy. *Rev. Mod. Phys.*, 15: 1–89, 1 1943. doi: 10.1103/RevModPhys.15.1. URL <https://link.aps.org/doi/10.1103/RevModPhys.15.1>.

K. Chen, T. Han, J. Gong, L. Bai, F. Ling, J.-J. Luo, X. Chen, L. Ma, T. Zhang, R. Su, Y. Ci, B. Li, X. Yang, and W. Ouyang. FengWu: Pushing the skillful global medium-range weather forecast beyond 10 days lead. *arXiv preprint arXiv:2304.02948*, 2023a.

L. Chen, X. Zhong, F. Zhang, Y. Cheng, Y. Xu, Y. Qi, and H. Li. Fuxi: A cascade machine learning forecasting system for 15-day global weather forecast, 2023b.

J. Coiffier. *Fundamentals of numerical weather prediction*. Cambridge University Press, 2011.

G. Danabasoglu, J.-F. Lamarque, J. Bacmeister, D. A. Bailey, A. K. DuVivier, J. Edwards, L. K. Emmons, J. Fasullo, R. Garcia, A. Gettelman, C. Hannay, M. M. Holland, W. G. Large, P. H. Lauritzen, D. M. Lawrence, J. T. M. Lenaerts, K. Lindsay, W. H. Lipscomb, M. J. Mills, R. Neale, K. W. Oleson, B. Otto-Bliesner, A. S. Phillips, W. Sacks, S. Tilmes, L. van Kampenhout, M. Vertenstein, A. Bertini, J. Dennis, C. Deser, C. Fischer, B. Fox-Kemper, J. E. Kay, D. Kinnison, P. J. Kushner, V. E. Larson, M. C. Long, S. Mickelson, J. K. Moore, E. Nienhouse, L. Polvani, P. J. Rasch, and W. G. Strand. The community earth system model version 2 (cesm2). *Journal of Advances in Modeling Earth Systems*, 12(2):e2019MS001916, 2020. doi: <https://doi.org/10.1029/2019MS001916>. URL <https://agupubs.onlinelibrary.wiley.com/doi/abs/10.1029/2019MS001916>. e2019MS001916 2019MS001916.

J. Degrave, F. Felici, J. Buchli, M. Neunert, B. Tracey, F. Carpanese, T. Ewalds, R. Hafner, A. Abdolmaleki, D. de las Casas, C. Donner, L. Fritz, C. Galperti, A. Huber, J. Keeling, M. Tsimpoukelli, J. Kay, A. Merle, J.-M. Moret, S. Noury, F. Pesamosca, D. Pfau, O. Sauter, C. Sommariva, S. Coda, B. Duval, A. Fasoli, P. Kohli, K. Kavukcuoglu, D. Hassabis, and M. Riedmiller. Magnetic control of tokamak plasmas through deep reinforcement learning. *Nature*, 602(7897):414–419, Feb 2022. ISSN 1476-4687. doi: 10.1038/s41586-021-04301-9. URL <https://doi.org/10.1038/s41586-021-04301-9>.

J. Diquigiovanni, M. Fontana, and S. Vantini. Conformal prediction bands for multivariate functional data, 2021.

K. L. Ebi, J. Vanos, J. W. Baldwin, J. E. Bell, D. M. Hondula, N. A. Errett, K. Hayes, C. E. Reid, S. Saha, J. Spector, and P. Berry. Extreme weather and climate change: Population health and health system implications. *Annu Rev Public Health*, 42:293–315, Jan. 2021.

Y. Gal and Z. Ghahramani. Dropout as a bayesian approximation: Representing model uncertainty in deep learning. In *International Conference on Machine Learning*, 2016.

N. Geneva and N. Zabaras. Modeling the dynamics of pde systems with physics-constrained deep auto-regressive networks. *Journal of Computational Physics*, 403: 109056, 2020. ISSN 0021-9991. doi: <https://doi.org/10.1016/j.jcp.2019.109056>. URL <https://www.sciencedirect.com/science/article/pii/S0021999119307612>.

N. Geneva and N. Zabaras. Transformers for modeling physical systems. *Neural Networks*, 146:272–289, 2022. ISSN 0893-6080. doi: <https://doi.org/10.1016/j.neunet.2021.11.022>. URL <https://www.sciencedirect.com/science/article/pii/S0893608021004500>.

G. Giudicelli, A. Lindsay, L. Harbour, C. Icenhour, M. Li, J. E. Hansel, P. German, P. Behne, O. Marin, R. H. Stogner, J. M. Miller, D. Schwen, Y. Wang, L. Munday, S. Schunert, B. W. Spencer, D. Yushu, A. Recuero, Z. M. Prince, M. Nezdyur, T. Hu, Y. Miao, Y. S. Jung, C. Matthews, A. Novak, B. Langley, T. Truster, N. Nobre, B. Alger,

D. Andrš, F. Kong, R. Carlsen, A. E. Slaughter, J. W. Peterson, D. Gaston, and C. Permann. 3.0 - MOOSE: Enabling massively parallel multiphysics simulations. *SoftwareX*, 26:101690, 2024. ISSN 2352-7110. doi: <https://doi.org/10.1016/j.softx.2024.101690>. URL <https://www.sciencedirect.com/science/article/pii/S235271102400061X>.

V. Gopakumar and D. Samaddar. Image mapping the temporal evolution of edge characteristics in tokamaks using neural networks. *Machine Learning: Science and Technology*, 1(1):015006, 2020. doi: 10.1088/2632-2153/ab5639. URL <https://dx.doi.org/10.1088/2632-2153/ab5639>.

V. Gopakumar, S. Pamela, and D. Samaddar. Loss landscape engineering via data regulation on pinns. *Machine Learning with Applications*, 12:100464, 2023. ISSN 2666-8270. doi: <https://doi.org/10.1016/j.mlwa.2023.100464>. URL <https://www.sciencedirect.com/science/article/pii/S2666827023000178>.

V. Gopakumar, S. Pamela, L. Zanisi, Z. Li, A. Gray, D. Brennand, N. Bhatia, G. Stathopoulos, M. Kusner, M. P. Deisenroth, A. Anandkumar, the JOREK Team, and M. Team. Plasma surrogate modelling using fourier neural operators. *Nuclear Fusion*, 64(5):056025, 4 2024. doi: 10.1088/1741-4326/ad313a. URL <https://dx.doi.org/10.1088/1741-4326/ad313a>.

A. Graubner, K. Kamyar Azizzadenesheli, J. Pathak, M. Mardani, M. Pritchard, K. Kashinath, and A. Anandkumar. Calibration of large neural weather models. In *NeurIPS 2022 Workshop on Tackling Climate Change with Machine Learning*, 2022.

J. K. Gupta and J. Brandstetter. Towards multi-spatiotemporal-scale generalized PDE modeling. *Transactions on Machine Learning Research*, 2023. ISSN 2835-8856. URL <https://openreview.net/forum?id=dPSTDbGtBY>.

W. Hackbusch. *The Poisson Equation*, pages 29–42. Springer, Berlin, Heidelberg, 2017. ISBN 978-3-662-54961-2. doi: 10.1007/978-3-662-54961-2_3. URL https://doi.org/10.1007/978-3-662-54961-2_3.

C. Ham, A. Kirk, and K. Veruagh. Insights on disruption physics in mast using high speed visible camera data. In *IAEA Second Technical Meeting on Plasma Disruptions and their Mitigation*, 2022. URL <https://conferences.iaea.org/event/281/contributions/24423/>.

Z. Hao, C. Su, S. Liu, J. Berner, C. Ying, H. Su, A. Anandkumar, J. Song, and J. Zhu. Dpot: Auto-regressive denoising operator transformer for large-scale pde pre-training, 2024.

S. Haykin. *Neural Networks: A Comprehensive Foundation*. Prentice Hall PTR, 1994.

K. He, X. Zhang, S. Ren, and J. Sun. Deep residual learning for image recognition. In *IEEE Conference on Computer Vision and Pattern Recognition*, 2016. doi: 10.1109/CVPR.2016.90.

H. Hersbach, B. Bell, P. Berrisford, S. Hirahara, A. Horányi, J. Muñoz-Sabater, J. Nicolas, C. Peubey, R. Radu, D. Schepers, A. Simmons, C. Soci, S. Abdalla, X. Abellán, G. Balsamo, P. Bechtold, G. Biavati, J. Bidlot, M. Bonavita, G. De Chiara, P. Dahlgren, D. Dee, M. Diamantakis, R. Dragani, J. Flemming, R. Forbes, M. Fuentes, A. Geer, L. Haimberger, S. Healy, R. J. Hogan, E. Hólm, M. Janisková, S. Keeley, P. Laloyaux, P. Lopez, C. Lupu, G. Radnoti, P. de Rosnay, I. Rozum, F. Vamborg, S. Villaume, and J.-N. Thépaut. The ERA5 global reanalysis. *Quarterly Journal of the Royal Meteorological Society*, 2020.

G. E. Hinton and R. Salakhutdinov. Reducing the dimensionality of data with neural networks. *Science*, 313(5786):504–507, 2006. doi: 10.1126/science.1127647. URL <https://www.science.org/doi/abs/10.1126/science.1127647>.

M. Hoelzl, G. T. A. Huijsmans, S. J. P. Pamela, M. Bécoulet, E. Nardon, F. Artola, B. Nkonga, C. V. Atanasiu, V. Bandaru, A. Bhole, D. Bonfiglio, A. Cathey, O. Czarny, A. Dvornova, T. Fehér, A. Fil, E. Franck, S. Futatani, M. Gruca, H. Guillard, J. W. Haverkort, I. Holod, D. Hu, S. K. Kim, S. Q. Korving, L. Kos, I. Krebs, L. Kripner, G. Latu, F. Liu, P. Merkel, D. Meshcheriakov, V. Mitterauer, S. Mochalskyy, J. A. Morales, R. Nies, N. Nikulsin, F. Orain, J. Pratt, R. Ramasamy, P. Ramet, C. Reux, K. Särkimäki, N. Schwarz, P. S. Verma, S. F. Smith, C. Sommariva, E. Strumberger, D. C. van Vugt, M. Verbeek, E. Westerhof, F. Wieschollek, and J. Zielinski. The jorek non-linear extended mhd code and applications to large-scale instabilities and their control in magnetically confined fusion plasmas. *Nuclear Fusion*, 61(6):065001, 2021. doi: 10.1088/1741-4326/abf99f. URL <https://dx.doi.org/10.1088/1741-4326/abf99f>.

D. Hose and M. Hanss. A universal approach to imprecise probabilities in possibility theory. *International Journal of Approximate Reasoning*, 133:133–158, 2021.

Hospital, Adam, J. R. Goñi, M. Orozco, and J. L. Gelpí. Molecular dynamics simulations: advances and applications. *Adv Appl Bioinform Chem*, 8:37–47, Nov. 2015.

Y. Hu, L. Chen, Z. Wang, and H. Li. Swinrvnn: A data-driven ensemble forecasting model via learned distribution perturbation. *Journal of Advances in Modeling Earth Systems*, 15(2):e2022MS003211, 2023. doi: <https://doi.org/10.1029/2022MS003211>. URL <https://agupubs.onlinelibrary.wiley.com/doi/abs/10.1029/2022MS003211.e2022MS003211> 2022MS003211.

C. M. Jiang, S. Esmaeilzadeh, K. Azizzadenesheli, K. Kashinath, M. Mustafa, H. A. Tchelepi, P. Marcus, Prabhat, and A. Anandkumar. Meshfreeflownet: A physics-constrained deep continuous space-time super-resolution framework. *arXiv:2005.01463*, 2020.

U. Johansson, H. Boström, and T. Löfström. Investigating normalized conformal regressors. In *2021 IEEE Symposium Series on Computational Intelligence (SSCI)*, pages 01–08, 2021. doi: 10.1109/SSCI50451.2021.9659853.

E. Kalnay. *Atmospheric Modeling, Data Assimilation and Predictability*. Cambridge University Press, 2002.

G. E. Karniadakis, I. G. Kevrekidis, L. Lu, P. Perdikaris, S. Wang, and L. Yang. Physics-informed machine learning. *Nature Reviews Physics*, 3(6):422–440, 2021. ISSN 2522-5820. doi: 10.1038/s42254-021-00314-5. URL <https://doi.org/10.1038/s42254-021-00314-5>.

J. Kates-Harbeck, A. Svyatkovskiy, and W. Tang. Predicting disruptive instabilities in controlled fusion plasmas through deep learning. *Nature*, 568(7753):526–531, Apr 2019. ISSN 1476-4687. doi: 10.1038/s41586-019-1116-4. URL <https://doi.org/10.1038/s41586-019-1116-4>.

R. Keisler. Forecasting global weather with graph neural networks. *arXiv preprint arXiv:2202.07575*, 2022.

D. P. Kingma and J. Ba. Adam: A method for stochastic optimization. In Y. Bengio and Y. LeCun, editors, *3rd International Conference on Learning Representations, ICLR 2015, San Diego, CA, USA, May 7-9, 2015, Conference Track Proceedings*, 2015. URL <http://arxiv.org/abs/1412.6980>.

A. Kirk, N. B. Ayed, G. Counsell, B. Dudson, T. Eich, A. Herrmann, B. Koch, R. Martin, A. Meakins, S. Saarelma, R. Scannell, S. Tallents, M. Walsh, H. R. Wilson, and the MAST team. Filament structures at the plasma edge on mast. *Plasma Physics and Controlled Fusion*, 48(12B):B433, nov 2006. doi: 10.1088/0741-3335/48/12B/S41. URL <https://dx.doi.org/10.1088/0741-3335/48/12B/S41>.

J. Knight. Safety critical systems: challenges and directions. In *Proceedings of the 24th International Conference on Software Engineering. ICSE 2002*, pages 547–550, 2002.

R. Koenker. *Quantile Regression*. Econometric Society Monographs. Cambridge University Press, 2005. doi: 10.1017/CBO9780511754098.

T. Kurth, S. Subramanian, P. Harrington, J. Pathak, M. Mardani, D. Hall, A. Miele, K. Kashinath, and A. Anandkumar. Fourcastnet: Accelerating global high-resolution weather forecasting using adaptive fourier neural operators. In *Proceedings of the Platform for Advanced Scientific Computing Conference, PASC '23*, New York, NY, USA, 2023. Association for Computing Machinery. ISBN 9798400701900. doi: 10.1145/3592979.3593412. URL <https://doi.org/10.1145/3592979.3593412>.

B. Lakshminarayanan, A. Pritzel, and C. Blundell. Simple and scalable predictive uncertainty estimation using deep ensembles, 2017.

E. R. Lalonde, B. Vischschraper, G. Bitsuamlak, and K. Dai. Comparison of neural network types and architectures for generating a surrogate aerodynamic wind turbine blade model. *Journal of Wind Engineering and Industrial Aerodynamics*, 216: 104696, 2021. ISSN 0167-6105. doi: <https://doi.org/10.1016/j.jweia.2021.104696>. URL <https://www.sciencedirect.com/science/article/pii/S0167610521001793>.

R. Lam, A. Sanchez-Gonzalez, M. Willson, P. Wirnsberger, M. Fortunato, F. Alet, S. Ravuri, T. Ewalds, Z. Eaton-Rosen, W. Hu, A. Merose, S. Hoyer, G. Holland, O. Vinyals, J. Stott, A. Pritzel, S. Mohamed, and P. Battaglia. Learning skillful

medium-range global weather forecasting. *Science*, 382(6677):1416–1421, 2023. doi: 10.1126/science.adi2336. URL <https://www.science.org/doi/abs/10.1126/science.adi2336>.

A. Lavin, D. Krakauer, H. Zenil, J. Gottschlich, T. Mattson, J. Brehmer, A. Anandkumar, S. Choudry, K. Rocki, A. G. Baydin, C. Prunkl, B. Paige, O. Isayev, E. Peterson, P. L. McMahon, J. Macke, K. Cranmer, J. Zhang, H. Wainwright, A. Hanuka, M. Veloso, S. Assefa, S. Zheng, and A. Pfeffer. Simulation intelligence: Towards a new generation of scientific methods. *arXiv:2112.03235*, 2021. doi: 10.48550/ARXIV.2112.03235. URL <https://arxiv.org/abs/2112.03235>.

J. Lei, M. G’Sell, A. Rinaldo, R. J. Tibshirani, and L. Wasserman. Distribution-free predictive inference for regression. *Journal of the American Statistical Association*, 113(523):1094–1111, 2018. doi: 10.1080/01621459.2017.1307116. URL <https://doi.org/10.1080/01621459.2017.1307116>.

D. Lerede, M. Nicoli, L. Savoldi, and A. Trotta. Analysis of the possible contribution of different nuclear fusion technologies to the global energy transition. *Energy Strategy Reviews*, 49:101144, 2023. ISSN 2211-467X. doi: <https://doi.org/10.1016/j.esr.2023.101144>. URL <https://www.sciencedirect.com/science/article/pii/S2211467X23000949>.

Z. Li, N. B. Kovachki, K. Azizzadenesheli, B. liu, K. Bhattacharya, A. Stuart, and A. Anandkumar. Fourier neural operator for parametric partial differential equations. In *International Conference on Learning Representations*, 2021. URL <https://openreview.net/forum?id=c8P9NQVtmn0>.

Z. Li, N. B. Kovachki, C. Choy, B. Li, J. Kossaifi, S. P. Otta, M. A. Nabian, M. Stadler, C. Hundt, K. Azizzadenesheli, and A. Anandkumar. Geometry-informed neural operator for large-scale 3d PDEs. In *Thirty-seventh Conference on Neural Information Processing Systems*, 2023a. URL <https://openreview.net/forum?id=86dXbqT5Ua>.

Z. Li, K. Meidani, and A. B. Farimani. Transformer for partial differential equations’ operator learning. *Transactions on Machine Learning Research*, 2023b. ISSN 2835-8856. URL <https://openreview.net/forum?id=EPPqt3uERT>.

J. Linke, J. Du, T. Loewenhoff, G. Pintsuk, B. Spilker, I. Steudel, and M. Wirtz. Challenges for plasma-facing components in nuclear fusion. *Matter and Radiation at Extremes*, 4(5):056201, 08 2019. ISSN 2468-2047. doi: 10.1063/1.5090100. URL <https://doi.org/10.1063/1.5090100>.

Z. Ma, K. Azizzadenesheli, and A. Anandkumar. Calibrated uncertainty quantification for operator learning via conformal prediction. *arXiv preprint arXiv:2402.01960*, 2024.

D. J. C. MacKay. A Practical Bayesian Framework for Backpropagation Networks. *Neural Computation*, 4(3):448–472, 05 1992. ISSN 0899-7667. doi: 10.1162/neco.1992.4.3.448. URL <https://doi.org/10.1162/neco.1992.4.3.448>.

R. Martin. False confidence, non-additive beliefs, and valid statistical inference. *International Journal of Approximate Reasoning*, 113:39–73, 2019.

M. McCabe, B. R.-S. Blanckard, L. Parker, R. Ohana, M. Cranmer, A. Bietti, M. Eickenberg, S. Golkar, G. Krawezik, F. Lanusse, M. Pettee, T. Tesileanu, K. Cho, and S. Ho. Multiple physics pretraining for physical surrogate models. In *NeurIPS 2023 AI for Science Workshop*, 2023. URL <https://openreview.net/forum?id=M121mQKuxa>.

S. Messoudi, S. Destercke, and S. Rousseau. Copula-based conformal prediction for multi-target regression. *Pattern Recognition*, 120:108101, 2021. ISSN 0031-3203. doi: <https://doi.org/10.1016/j.patcog.2021.108101>. URL <https://www.sciencedirect.com/science/article/pii/S0031320321002880>.

S. Messoudi, S. Destercke, and S. Rousseau. Ellipsoidal conformal inference for multi-target regression. In U. Johansson, H. Boström, K. An Nguyen, Z. Luo, and L. Carlsson, editors, *Proceedings of the Eleventh Symposium on Conformal and Probabilistic Prediction with Applications*, volume 179 of *Proceedings of Machine Learning Research*, pages 294–306. PMLR, 24–26 Aug 2022. URL <https://proceedings.mlr.press/v179/messoudi22a.html>.

M. Müller, M. Homleid, K.-I. Ivarsson, M. A. Ø. Køltzow, M. Lindskog, K. H. Midtbø, U. Andrae, T. Aspelien, L. Berggren, D. Bjørge, P. Dahlgren, J. Kristiansen, R. Randriamampianina, M. Ridal, and O. Vignes. AROME-MetCoOp: A nordic convective-scale operational weather prediction model. *Weather and Forecasting*, 2017.

P. Mánek, G. V. Goffrier, V. Gopakumar, N. Nikolaou, J. Shimwell, and I. Waldmann. Fast regression of the tritium breeding ratio in fusion reactors. *Machine Learning: Science and Technology*, 4(1):015008, 2023. doi: 10.1088/2632-2153/acb2b3. URL <https://doi.org/10.1088/2632-2153/acb2b3>.

T. Nguyen, J. Brandstetter, A. Kapoor, J. K. Gupta, and A. Grover. Climax: A foundation model for weather and climate, 2023.

J. Oskarsson, T. Landelius, M. P. Deisenroth, and F. Lindsten. Probabilistic weather forecasting with hierarchical graph neural networks. *arXiv preprint arXiv:2406.04759*, 2024.

S. J. P. Pamela, N. Carey, J. Brandstetter, R. Akers, L. Zanisi, J. Buchanan, V. Gopakumar, M. Hoelzl, G. Huijsmans, K. Pentland, T. James, G. Antonucci, and the JOREK Team. Neural-parareal: Dynamically training neural operators as coarse solvers for time-parallelisation of fusion mhd simulations, 2024. URL <https://arxiv.org/abs/2405.01355>.

H. Papadopoulos. Inductive conformal prediction: Theory and application to neural networks. In P. Fritzsche, editor, *Tools in Artificial Intelligence*, chapter 18. IntechOpen, Rijeka, 2008. doi: 10.5772/6078.

T. Pfaff, M. Fortunato, A. Sanchez-Gonzalez, and P. Battaglia. Learning mesh-based simulation with graph networks. In *International Conference on Learning Representations*, 2021. URL https://openreview.net/forum?id=roNqYL0_XP.

I. Price, A. Sanchez-Gonzalez, F. Alet, T. Ewalds, A. El-Kadi, J. Stott, S. Mohamed, P. Battaglia, R. Lam, and M. Willson. Gencast: Diffusion-based ensemble forecasting for medium-range weather. *arXiv preprint arXiv:2312.15796*, 2023.

A. F. Psaros, X. Meng, Z. Zou, L. Guo, and G. E. Karniadakis. Uncertainty quantification in scientific machine learning: Methods, metrics, and comparisons. *Journal of Computational Physics*, 477:111902, 2023. ISSN 0021-9991. doi: <https://doi.org/10.1016/j.jcp.2022.111902>. URL <https://www.sciencedirect.com/science/article/pii/S0021999122009652>.

J. Quionero-Candela, M. Sugiyama, A. Schwaighofer, and N. D. Lawrence. *Dataset Shift in Machine Learning*. The MIT Press, 2009. ISBN 0262170051.

M. A. Rahman, R. J. George, M. Elleithy, D. Leibovici, Z. Li, B. Bonev, C. White, J. Berner, R. A. Yeh, J. Kossaifi, K. Azizzadenesheli, and A. Anandkumar. Pretraining codomain attention neural operators for solving multiphysics pdes, 2024.

S. Rasp, S. Hoyer, A. Merose, I. Langmore, P. Battaglia, T. Russel, A. Sanchez-Gonzalez, V. Yang, R. Carver, S. Agrawal, M. Chantry, Z. B. Bouallegue, P. Dueben, C. Bromberg, J. Sisk, L. Barrington, A. Bell, and F. Sha. Weatherbench 2: A benchmark for the next generation of data-driven global weather models, 2024.

Y. Romano, E. Patterson, and E. Candes. Conformalized quantile regression. In H. Wallach, H. Larochelle, A. Beygelzimer, F. d'Alché-Buc, E. Fox, and R. Garnett, editors, *Advances in Neural Information Processing Systems*, volume 32. Curran Associates, Inc., 2019. URL https://proceedings.neurips.cc/paper_files/paper/2019/file/5103c3584b063c431bd1268e9b5e76fb-Paper.pdf.

O. Ronneberger, P. Fischer, and T. Brox. U-net: Convolutional networks for biomedical image segmentation. In N. Navab, J. Hornegger, W. M. Wells, and A. F. Frangi, editors, *Medical Image Computing and Computer-Assisted Intervention – MICCAI 2015*, pages 234–241, Cham, 2015. Springer International Publishing. ISBN 978-3-319-24574-4.

A. Sanchez-Gonzalez, J. Godwin, T. Pfaff, R. Ying, J. Leskovec, and P. Battaglia. Learning to simulate complex physics with graph networks. In H. D. III and A. Singh, editors, *Proceedings of the 37th International Conference on Machine Learning*, volume 119 of *Proceedings of Machine Learning Research*, pages 8459–8468. PMLR, 07 2020. URL <https://proceedings.mlr.press/v119/sanchez-gonzalez20a.html>.

F. Scarselli, M. Gori, A. C. Tsoi, M. Hagenbuchner, and G. Monfardini. The graph neural network model. *IEEE Transactions on Neural Networks*, 20(1):61–80, 2009. doi: 10.1109/TNN.2008.2005605.

G. Shafer and V. Vovk. A tutorial on conformal prediction. *Journal of Machine Learning Research*, 9(3), 2008.

A. Sheshadri, M. Borrus, M. Yoder, and T. Robinson. Midlatitude error growth in atmospheric gcms: The role of eddy growth rate. *Geophysical Research Letters*, 48(23):e2021GL096126, 2021. doi: <https://doi.org/10.1029/2021GL096126>.

URL <https://agupubs.onlinelibrary.wiley.com/doi/abs/10.1029/2021GL096126>.
 e2021GL096126 2021GL096126.

K. Shukla, V. Oommen, A. Peyvan, M. Penwarden, N. Plewacki, L. Bravo, A. Ghoshal, R. M. Kirby, and G. E. Karniadakis. Deep neural operators as accurate surrogates for shape optimization. *Engineering Applications of Artificial Intelligence*, 129:107615, 2024. ISSN 0952-1976. doi: <https://doi.org/10.1016/j.engappai.2023.107615>. URL <https://www.sciencedirect.com/science/article/pii/S0952197623017992>.

K. Stankewiciute, A. M. Alaa, and M. van der Schaar. Conformal time-series forecasting. In M. Ranzato, A. Beygelzimer, Y. Dauphin, P. Liang, and J. W. Vaughan, editors, *Advances in Neural Information Processing Systems*, volume 34, pages 6216–6228. Curran Associates, Inc., 2021. URL https://proceedings.neurips.cc/paper_files/paper/2021/file/312f1ba2a72318edaaa995a67835fad5-Paper.pdf.

S. Sun. Conformal methods for quantifying uncertainty in spatiotemporal data: A survey, 2022.

M. Takamoto, T. Praditia, R. Leiteritz, D. MacKinlay, F. Alesiani, D. Pflüger, and M. Niepert. Pdebench: An extensive benchmark for scientific machine learning. *arXiv:2210.07182*, 2022. doi: 10.18419/darus-2986. URL <https://doi.org/10.18419/darus-2986>.

R. J. Tibshirani, R. Foygel Barber, E. Candes, and A. Ramdas. Conformal prediction under covariate shift. *Advances in Neural Information Processing Systems*, 2019.

. Tipler, Paul Allen. *Physics for scientists and engineers. Volume 1, Mechanics, oscillations and waves, thermodynamics*. Sixth edition. New York : W.H. Freeman, [2008] ©2008, 2008. URL <https://search.library.wisc.edu/catalog/9910077755502121>. Contains chapters 1-20, R of complete sixth edition.;Includes bibliographical references and index.

K. L. van de Plassche, J. Citrin, C. Bourdelle, Y. Camenen, F. J. Casson, V. I. Dagnelie, F. Felici, A. Ho, and S. V. M. and. Fast modeling of turbulent transport in fusion plasmas using neural networks. *Physics of Plasmas*, 27(2):022310, 2020. doi: 10.1063/1.5134126. URL <https://doi.org/10.10632F1.5134126>.

V. Vovk. Conditional validity of inductive conformal predictors. In *Asian Conference on Machine Learning*, 2012.

V. Vovk, A. Gammerman, and G. Shafer. *Algorithmic Learning in a Random World*. Springer, 2005.

N. Walkden, F. Riva, J. Harrison, F. Militello, T. Farley, J. Omotani, and B. Lipschultz. The physics of turbulence localised to the tokamak divertor volume. *Communications Physics*, 5(1):139, Jun 2022. ISSN 2399-3650. doi: 10.1038/s42005-022-00906-2. URL <https://doi.org/10.1038/s42005-022-00906-2>.

G. Wen, Z. Li, Q. Long, K. Azizzadenesheli, A. Anandkumar, and S. M. Benson. Real-time high-resolution CO₂ geological storage prediction using nested fourier neural operators. *Energy & Environmental Science*, 16(4):1732–1741, 2023. doi: 10.1039/d2ee04204e. URL <https://doi.org/10.10392Fd2ee04204e>.

C. Xu and Y. Xie. Conformal prediction interval for dynamic time-series. In M. Meila and T. Zhang, editors, *Proceedings of the 38th International Conference on Machine Learning*, volume 139 of *Proceedings of Machine Learning Research*, pages 11559–11569. PMLR, 18–24 Jul 2021. URL <https://proceedings.mlr.press/v139/xu21h.html>.

C. Xu, Y. Xie, D. A. Z. Vazquez, R. Yao, and F. Qiu. Spatio-temporal wildfire prediction using multi-modal data. *IEEE Journal on Selected Areas in Information Theory*, 4:302–313, 2023. doi: 10.1109/JSAIT.2023.3276054.

H. Yin, A. Vahdat, J. Alvarez, A. Mallya, J. Kautz, and P. Molchanov. A-ViT: Adaptive tokens for efficient vision transformer. In *Proceedings of the IEEE/CVF Conference on Computer Vision and Pattern Recognition*, 2022a.

H. Yin, A. Vahdat, J. M. Alvarez, A. Mallya, J. Kautz, and P. Molchanov. A-vit: Adaptive tokens for efficient vision transformer. In *Proceedings of the IEEE/CVF Conference on Computer Vision and Pattern Recognition (CVPR)*, pages 10809–10818, 06 2022b.

Z. Yin, R. Orozco, M. Louboutin, and F. J. Herrmann. Solving multiphysics-based inverse problems with learned surrogates and constraints. *Advanced Modeling and Simulation in Engineering Sciences*, 10(1), Oct. 2023. ISSN 2213-7467. doi: 10.1186/s40323-023-00252-0. URL <http://dx.doi.org/10.1186/s40323-023-00252-0>.

Z. Zou, X. Meng, A. F. Psaros, and G. E. Karniadakis. Neuraluq: A comprehensive library for uncertainty quantification in neural differential equations and operators. *SIAM Review*, 66(1):161–190, 2024. doi: 10.1137/22M1518189. URL <https://doi.org/10.1137/22M1518189>.

D. Zwicker. py-pde: A python package for solving partial differential equations. *Journal of Open Source Software*, 5(48):2158, 2020. doi: 10.21105/joss.02158. URL <https://doi.org/10.21105/joss.02158>.

Appendix A. Poisson Equation

The Poisson Equation in one-dimension takes the form:

$$\frac{\partial^2 u}{\partial x^2} = \rho, \quad x \in [0, 1], \quad (7)$$

where u defines the field value, x the spatial domain, and ρ the density of the source.

The Poisson equation is solved with a finite difference scheme using the *py-pde* python package (Zwicker, 2020). Equation (7) is constructed as an initial-value problem, where a scalar uniform field is initialised across the domain and evolved until convergence. A dataset comprising different instances of the 1D Poisson equation is constructed by sampling for different initial values uniformly from within the domain: $u_{\text{init}} \in [0, 4]$.

A total of 7,000 data points are generated, where 5,000 are used to train an MLP with 3 layers and 64 neurons in each layer, 1,000 are used to perform the calibration required to estimate the nonconformity scores and another 1,000 for validation. Being a steady-state problem, the MLP learns how a scalar field evolves under the influence of the Laplacian, mapping from the initial to the final state of evolution. The network learns to map the initial condition to the final steady-state solution.

Each MLP is trained to take in the scalar initial field along the 32-point spatial domain to output the final field at the steady state. For the case of STD, the architecture is modified with 1D dropout layers. Each model is trained for up to 1000 epochs using the Adam optimiser Kingma and Ba (2015) with a step-decaying learning rate. The learning rate is initially set to 0.005 and scheduled to decrease by half after every 100 epochs. The model was trained using a quantile loss for the case of CQR and MSE loss in all other cases.

Appendix B. Convection-Diffusion Equation

B.1 Physics

Consider a modified version of the one-dimensional convection-diffusion equation used to model the transport of a fluid:

$$\frac{\partial u}{\partial t} = D \frac{\partial^2 u}{\partial x^2} + u \frac{\partial D}{\partial x} - c \frac{\partial u}{\partial x}, \quad x \in [0, 10], t \in [0, 0.1] \quad (8)$$

$$u(x, t = 0) = \exp\left(-\frac{(x - \mu^2)}{2\sigma^2}\right). \quad (9)$$

Here u defines the density of the fluid, x the spatial coordinate, t the temporal coordinate, D the diffusion coefficient, and c the convection velocity. The initial condition is parameterised by μ and σ^2 , representing the mean and variance of a Gaussian distribution. The system is bounded by a no-flux boundary condition.

The numerical solution for the above equation is built using a Newtonian solver with a forward time centered space implementation in Python. We construct a dataset by Latin hypercube sampling across parameters D, c, μ, σ . Each parameter is sampled from within the domain given in Table 2 to generate 3,000 simulation points, each with its own initial condition, diffusion coefficient and convection velocity. We generate another 2,000 data points, 1,000 each for the calibration and procuring of the prediction sets. These datasets are built by sampling across a different domain of the diffusion coefficient and convection velocity, different from that used for training; see Table 3 for details. We use a one-dimensional U-Net to model the evolution of the convection-diffusion equation. The U-Net learns to perform the mapping from the first 10 time instances to the next 10 time instances, learning across the different field parameters and initial conditions. A more detailed physics description and the training set-up of the model can be found in Appendix B.

As discussed in section 3.2, the dataset is built by solving the one-dimensional Convection Diffusion equation numerically. The physics of the equation, given by the various coefficients is sampled from a certain range as given in Table 2. Each datapoint, as in each simulation is generated with different Diffusion coefficients and wave velocities as described in section 3.2. Each simulation is run for 100 time iterations with a $\Delta t = 0.0005$ across a spatial domain spanning $[0, 10]$, uniformly discretised into 200 spatial units in the x-axis. Once the simulations are run and the dataset is generated, we downsample the temporal discretisation from 100 to 20 by slicing across the domain. The sampling parameters governing the PDE solutions used for the training are given in Table 2 and that used for the calibration and prediction is given in Table 3.

B.2 Model and Training

We train a U-Net to map the spatio-temporal evolution of the field variable taking in the first 20 time instances (T_{in}) to the next 10 time instances (T_{out}). For the case of the Convection-Diffusion Equation, we don't deploy an auto-regressive structure but perform a mapping from the initial distribution to the later distribution. The U-Net architecture can be found in Table 4. For the case of STD, the architecture is modified with 1D dropout layers following each encoder and decoder of the U-Net. Though the values governing the evolution of Convection-Diffusion are relatively small, for better representation we normalise

Table 2: Domain range and sampling strategies across the coefficients and initial condition parameters for building the training dataset for the 1D convection-diffusion equation.

Parameter	Domain	Type
Diffusion Coefficient (α)	$[\sin(\frac{x}{\pi}), \sin(\frac{x}{2\pi})]$	Continuous
Convection velocity (β)	$[0.1, 0.5]$	Continuous
Mean (μ)	$[1.0, 8.0]$	Continuous
Variance (γ)	$[0.25, 0.75]$	Continuous

the value with a linear range scaling, allowing the field values to lie between -1 and 1. Each model is trained for up to 500 epochs using the Adam optimiser Kingma and Ba (2015) with a step decaying learning rate. The learning rate is initially set to 0.005 and scheduled to decrease by half after every 100 epochs. The model was trained using a quantile loss for the case of CQR and an MSE loss in all other cases.

Table 3: Domain range and sampling strategies across the coefficients and initial condition parameters for building the calibration and prediction datasets for the 1D convection-diffusion equation.

Parameter	Domain	Type
Diffusion Coefficient (α)	$[\sin(\frac{x}{2\pi}), \sin(\frac{x}{4\pi})]$	Continuous
Convection velocity (β)	$[0.5, 1, 0]$	Continuous
Mean (μ)	$[1.0, 8.0]$	Continuous
Variance (γ)	$[0.25, 0.75]$	Continuous

Table 4: Architecture of the 1D U-Net deployed for modelling 1D Convection-Diffusion Equation

Part	Layer	Output Shape
Input	-	(50, 20, 200)
Encoder 1	Conv1d/BatchNorm1d/Tanh	(50, 32, 200)
Pool 1	MaxPool1d	(50, 32, 200)
Encoder 2	Conv1d/BatchNorm1d/Tanh	(50, 64, 100)
Pool 2	MaxPool1d	(50, 64, 100)
Encoder 3	Conv1d/BatchNorm1d/Tanh	(50, 128, 50)
Pool 3	MaxPool1d	(50, 128, 50)
Encoder 4	Conv1d/BatchNorm1d/Tanh	(50, 256, 25)
Pool 4	MaxPool1d	(50, 256, 25)
Bottleneck	Conv1d/BatchNorm1d/Tanh	(50, 512, 12)
Decoder 4	ConvTranspose1d/Encoder 4	(50, 256, 25)
Decoder 3	ConvTranspose1d/Encoder 3	(50, 128, 50)
Decoder 2	ConvTranspose1d/Encoder 2	(50, 64, 100)
Decoder 1	ConvTranspose1d/Encoder 1	(50, 32, 200)
Rescale	Conv1d	(50, 10, 200)

Appendix C. Wave Equation

C.1 Physics

Consider the two-dimensional wave equation

$$\frac{\partial^2 u}{\partial t^2} = c^2 \left(\frac{\partial^2 u}{\partial x^2} + \frac{\partial^2 u}{\partial y^2} \right) = 0, \quad x, y \in [-1, 1], \quad t \in [0, 1] \quad (10)$$

$$u(x, y, t = 0) = \exp(-\alpha((x - \beta)^2 + (y - \gamma)^2)) \quad (11)$$

$$\frac{\partial u(x, y, t = 0)}{\partial t} = 0, \quad u(x, y, t) = 0, \quad x, y \in \partial\Omega, \quad t \in [0, 1], \quad (12)$$

where u defines the field variable, c the wave velocity, x and y the spatial coordinates, t the temporal coordinates. α , β and γ are variables that parameterise the initial condition of the PDE setup. There exists an additional constraint to the PDE setup that initialises the velocity of the wave to 0. The system is bounded periodically within the mentioned domain.

The solution for the wave equation is obtained by deploying a spectral solver that uses a leapfrog method for time discretisation and a Chebyshev spectral method on tensor product grid for spatial discretisation (Gopakumar et al., 2023). The dataset is built by performing a Latin hypercube scan across the defined domain for the parameters α, β, γ , which accounts for the amplitude and the location of the Gaussian peak, sampled differently for each simulation. We generate 2,500 simulation points, each one with its own initial condition and use 500 for training, 1,000 each for calibration and procuring the prediction sets. We train a 2D U-Net and an FNO to learn the evolution of wave dynamics.

The physics of the equation, given by the various coefficients is held constant across the dataset generation throughout as given in Equation (10). Each data point, as in each simulation is generated with a different initial condition as described above. The parameters of the initial conditions are sampled from within the domain as given in Table 5. Each simulation is run for 150-time iterations with a $\Delta t = 0.00667$ across a spatial domain spanning $[-1, 1]^2$, uniformly discretised into 33 spatial units in the x and y axes. Once the simulations are completed and the dataset is generated, we select the first 80 time instances of the evolution of each simulation to be used for training.

Table 5: Domain range and sampling strategies across the initial condition parameters for the 2D Wave Equation. A 2D Gaussian peak with a given amplitude and position within the domain is sampled using a Latin hypercube.

Parameter	Domain	Type
Amplitude (α)	[10, 50]	Continuous
X position (β)	[0.1, 0.5]	Continuous
Y position (γ)	[0.1, 0.5]	Continuous

C.2 Model and Training

We train U-Nets and FNOs to map the spatio-temporal evolution of the field variables. For the U-Nets, the network takes in the first 20 time instances (T_{in}) to map the next 30 time instances ($step$). The U-net performs a feed-forward mapping without any autoregressive rollouts. For the FNO we deploy an auto-regressive structure that performs time rollouts allowing us to map the initial time steps in a recursive manner up until the desired time instance (T_{out}). Each model autoregressively models the evolution of the field variable up until the 80th time instance. The U-Net architecture can be found in Table 6 and the FNO in Table 7. For the case of STD, the architecture is modified with 2D dropout layers following each encoder and decoder of the U-Net and after each Fourier layer within the FNO. We employ a linear range normalisation scheme, placing the field values between -1 and 1. Each model is trained for up to 500 epochs using the Adam optimiser (Kingma and Ba, 2015) with a step decaying learning rate. The learning rate is initially set to 0.005 and scheduled to decrease by half after every 100 epochs. The model was trained using a quantile loss in the case of CQR and an MSE loss in the other cases.

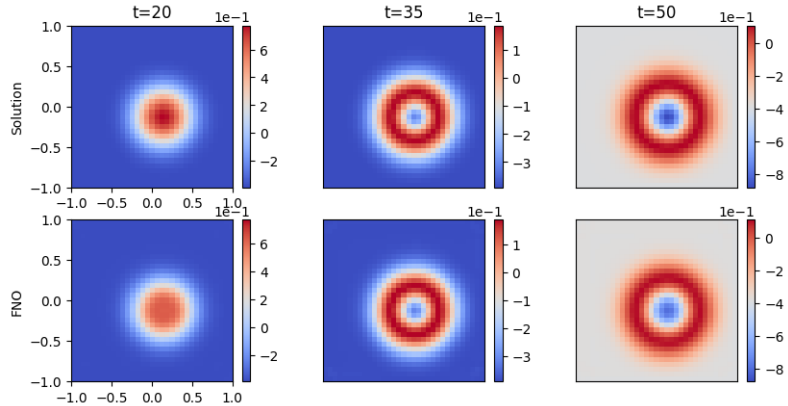


Figure 24: Waves: Temporal evolution of field associated with the wave equation modelled using the numerical spectral solver (top of the figure) and that of the U-Net (bottom of the figure). The spatial domain is given in Cartesian geometry.

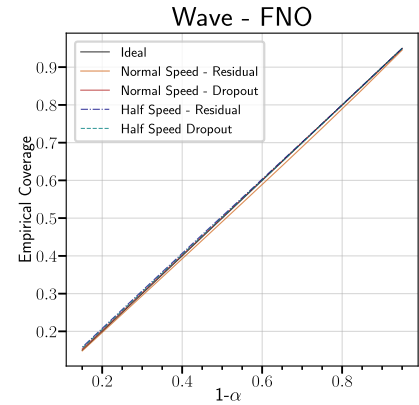


Figure 23: Coverage observed using AER and STD across datasets with normal wave speed (in-distribution) and half speed (out-distribution).

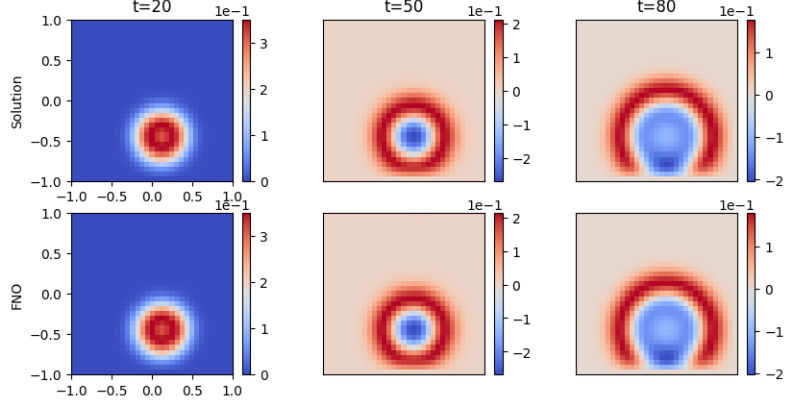


Figure 25: Waves: Temporal evolution of field associated with the wave equation modelled using the numerical spectral solver (top of the figure) and that of the FNO (bottom of the figure). The spatial domain is given in Cartesian geometry.

Table 6: Architecture of the 2D U-Net deployed for the 2D Wave Equation

Part	Layer	Output Shape
Input	-	(50, 20, 33, 33)
Encoder 1	Conv2d/BatchNorm2d/Tanh	(50, 32, 33, 33)
Pool 1	MaxPool2d	(50, 32, 33, 33)
Encoder 2	Conv2d/BatchNorm2d/Tanh	(50, 64, 16, 16)
Pool 2	MaxPool2d	(50, 64, 16, 16)
Bottleneck	Conv2d/BatchNorm2d/Tanh	(50, 128, 8, 8)
Decoder 2	ConvTranspose2D/Encoder 2	(50, 64, 16, 16)
Decoder 1	ConvTranspose2D/Encoder 1	(50, 32, 33, 33)
Rescale	Conv2D	(50, 10, 33, 33)

Table 7: Architecture of the Individual FNO deployed for modelling the Wave Equation

Part	Layer	Output Shape
Input	-	(50, 33, 33, 22)
Lifting	Linear	(50, 33, 33, 32)
Fourier 1	Fourier2d/Conv2d/Add/GELU	(50, 32, 33, 33)
Fourier 2	Fourier2d/Conv2d/Add/GELU	(50, 32, 33, 33)
Fourier 3	Fourier2d/Conv2d/Add/GELU	(50, 32, 33, 33)
Fourier 4	Fourier2d/Conv2d/Add/GELU	(50, 32, 33, 33)
Fourier 5	Fourier2d/Conv2d/Add/GELU	(50, 32, 33, 33)
Fourier 6	Fourier2d/Conv2d/Add/GELU	(50, 32, 33, 33)
Projection 1	Linear	(50, 33, 33, 128)
Projection 2	Linear	(50, 33, 33, 10)

Appendix D. Navier-Stokes Equations for Vorticity

D.1 Physics

The Navier-Stokes scenario that we are interested in modelling is taken from the exact formulation in Li et al. (2021), where the viscosity of the incompressible fluid in 2D is expressed as:

$$\frac{\partial w}{\partial t} + u \nabla w = \nu \nabla^2 w + f, \quad x \in (0, 1), y \in (0, 1), t \in (0, T) \quad (13)$$

$$\nabla u = 0, \quad x \in (0, 1), y \in (0, 1), t \in (0, T) \quad (14)$$

$$w = w_0, \quad x \in (0, 1), y \in (0, 1), t = 0, \quad (15)$$

where u is the velocity field and vorticity is the curl of the velocity field $w = \nabla \times u$. The domain is split across the spatial domain characterised by x, y and the temporal domain t . The initial vorticity is given by the field w_0 . The forcing function is given by f and is a function of the spatial domain in x, y . We utilise two datasets from Li et al. (2021) that are built by solving the above equations with viscosities $\nu = 1e - 3$ and $\nu = 1e - 4$ under different initial vorticity distributions. For further information on the physics and the data generation, refer Li et al. (2021).

D.2 Model and Training

We train an FNO to map the spatio-temporal evolution of the vorticity taking in the first 10 time instances (*T_in*) to the next 10 time instances (*step*). For the case of the Navier-Stokes equations, we deploy a feed-forward mapping from the initial 10 time steps to the next 10 time steps. The architecture for the FNO can be found in Table 8. We deploy a Min-Max normalisation strategy, allowing the field values to lie between -1 and 1. Each model is trained for up to 500 epochs using the Adam optimiser (Kingma and Ba, 2015) with a step decaying learning rate. The learning rate is initially set to 0.005 and scheduled to decrease by half after every 100 epochs. The model was trained using a relative LP loss. Considering the efficiency and simplicity, conformal prediction for the Navier-Stokes case was conducted using AER and STD as a nonconformity metric as given in the Section 2.2.

D.2.1 PREDICTION

Table 8: Architecture of the Individual FNO deployed for modelling the Navier-Stokes Equation

Part	Layer	Output Shape
Input	-	(20, 64, 64, 12)
Lifting	Linear	(50, 64, 64, 32)
Fourier 1	Fourier2d/Conv2d/Add/GELU	(20, 16, 64, 64)
Fourier 2	Fourier2d/Conv2d/Add/GELU	(20, 16, 64, 64)
Fourier 3	Fourier2d/Conv2d/Add/GELU	(20, 16, 64, 64)
Fourier 4	Fourier2d/Conv2d/Add/GELU	(20, 16, 64, 64)
Fourier 5	Fourier2d/Conv2d/Add/GELU	(20, 16, 64, 64)
Fourier 6	Fourier2d/Conv2d/Add/GELU	(20, 16, 64, 64)
Projection 1	Linear	(20, 64, 64, 128)
Projection 2	Linear	(20, 64, 64, 10)

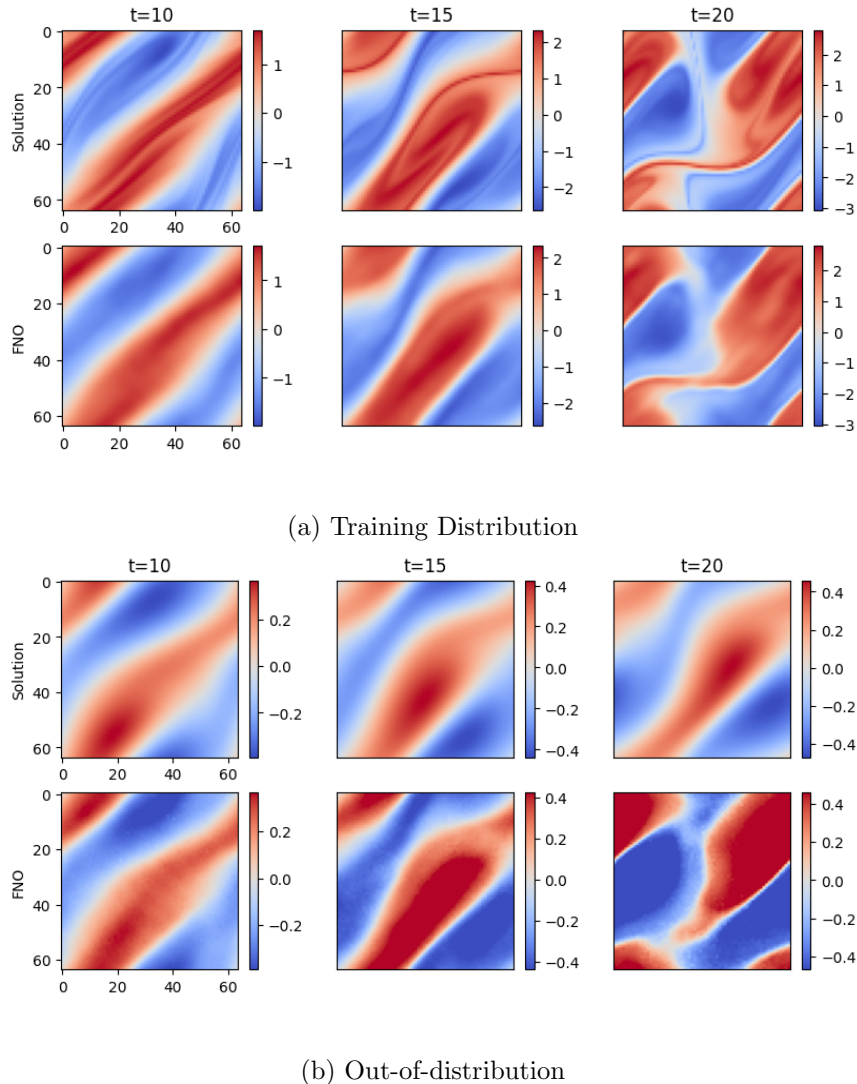


Figure 26: Navier–Stokes: Temporal evolution of the vorticity associated with the Navier–Stokes equations. In (a) we compare the FNO performance against that of the numerical solver within the training distribution ($\nu = 1e-3$). In (b) we demonstrate the performance of the same FNO on out-of-distribution data upon which we perform Conformal Prediction ($\nu = 1e-4$) modelled using the numerical solver (top of the figure) and that of the FNO (bottom of the figure). The spatial domain is given in Cartesian geometry.

Appendix E. Magnetohydrodynamics of Plasma Blobs

E.1 Physics

The Reduced-MHD equations that we are interested in modelling can be described as:

$$\frac{\partial \rho}{\partial t} = -\nabla \cdot (\rho \vec{v}) + D \nabla^2 \rho \quad (16)$$

$$\rho \frac{\partial \vec{v}}{\partial t} = -\rho \vec{v} \cdot \nabla \vec{v} - \nabla p + \mu \nabla^2 \vec{v} \quad (17)$$

$$\frac{\partial p}{\partial t} = -\vec{v} \cdot \nabla p - \gamma p \nabla \cdot \vec{v} + \kappa \nabla^2 T \quad (18)$$

where ρ is the density, p the pressure, T the temperature, and \vec{v} the velocity. D is the diffusion coefficient, μ the viscosity, and κ the thermal conductivity. The ratio of specific heats γ is taken to be that of a monatomic gas, $\frac{5}{3}$.

Equation (16) depicts the continuity equation, modelling the evolution of density subject to diffusion, convection and the electrostatic potential. Equation (17) represents the conservation of momentum within the field. Equation (18) models the conservation of energy, characterised by the pressure, temperature and velocity.

Within each simulation, multiple-density blobs with varying positions, width and amplitude are initialised in a low-density background. In the absence of a plasma current to hold the density blob in place, the pressure gradient term in the momentum equation generates a buoyancy effect, causing the blob to move outwards. The system under consideration is characterised by a highly correlated multi-variable setting as given above. Within each simulation, we evolve the blobs migrate radially outward until they reach the wall, where the Dirichlet boundary conditions engage to allow for convection and diffusion. Refer to (Gopakumar et al., 2024) for more detailed information about the setup.

Table 9: Domain range and sampling strategies across the initial condition parameters.

Parameter	Distribution	Type
Width	$U[0.02, 0.1]$	Continuous
Number of Blobs	$U[1, 10]$	Discrete
R - Position of Blobs	$U[9.4, 10.4]$	Continuous
Z - Position of Blobs	$U[-0.4, +0.4]$	Continuous
Amplitude of Density of Blobs	$U[0.5, 2.0]$	Continuous
Amplitude of Temperature of Blobs	$U[0.5, 3.0]$	Continuous

E.2 Model and Training

We train a multi-variable FNO to map the spatio-temporal evolution of the field variable taking in the first 10 time instances (T_{in}) to the next 5 time instances ($step$). For the case of the MHD equations, we deploy an auto-regressive structure that performs a time rollout allowing us to map the initial time steps in a recursive manner up until the desired time

instance (T_{out}). Each model autoregressively models the evolution of the field variable up until the 50th time instance. The architecture for the multi-variable FNO can be found in Table 10. We deploy a two-fold normalisation strategy considering the nature of the dataset. The physical field information represented within the MHD cases are in different scales, with densities ranging from 0 to 1e20 and temperatures ranging up to 1e6. Since we are considering the gradual diffusion of an inhomogeneous density blob(s), the data distribution within the spatial domain is severely imbalanced. Taking these aspects of the training data into consideration, a physics normalisation is performed initially, where the field values are scaled down by dividing against the prominent field value. This is followed up by a linear range scaling, allowing the field values to lie between -1 and 1. Each model is trained for up to 500 epochs using the Adam optimiser (Kingma and Ba, 2015) with a step decaying learning rate. The learning rate is initially set to 0.005 and scheduled to decrease by half after every 100 epochs. The model was trained using a relative LP loss. Considering the efficiency and simplicity, conformal prediction for the MHD case was only conducted using the AER as a nonconformity metric as given in the Section 2.2.

Table 10: Architecture of the Multi-variable FNO deployed for modelling Reduced MHD.

Part	Layer	Output Shape
Input	-	(10, 3, 106, 106, 12)
Lifting	Linear	(10, 3, 106, 106, 32)
Fourier 1	Fourier2d/Conv3d/Add/GELU	(10, 3, 32, 106, 106)
Fourier 2	Fourier2d/Conv3d/Add/GELU	(10, 3, 32, 106, 106)
Fourier 3	Fourier2d/Conv3d/Add/GELU	(10, 3, 32, 106, 106)
Fourier 4	Fourier2d/Conv3d/Add/GELU	(10, 3, 32, 106, 106)
Fourier 5	Fourier2d/Conv3d/Add/GELU	(10, 3, 32, 106, 106)
Fourier 6	Fourier2d/Conv3d/Add/GELU	(10, 3, 32, 106, 106)
Projection 1	Linear	(10, 3, 106, 106, 128)
Projection 2	Linear	(10, 3, 106, 106, 5)

E.3 Prediction

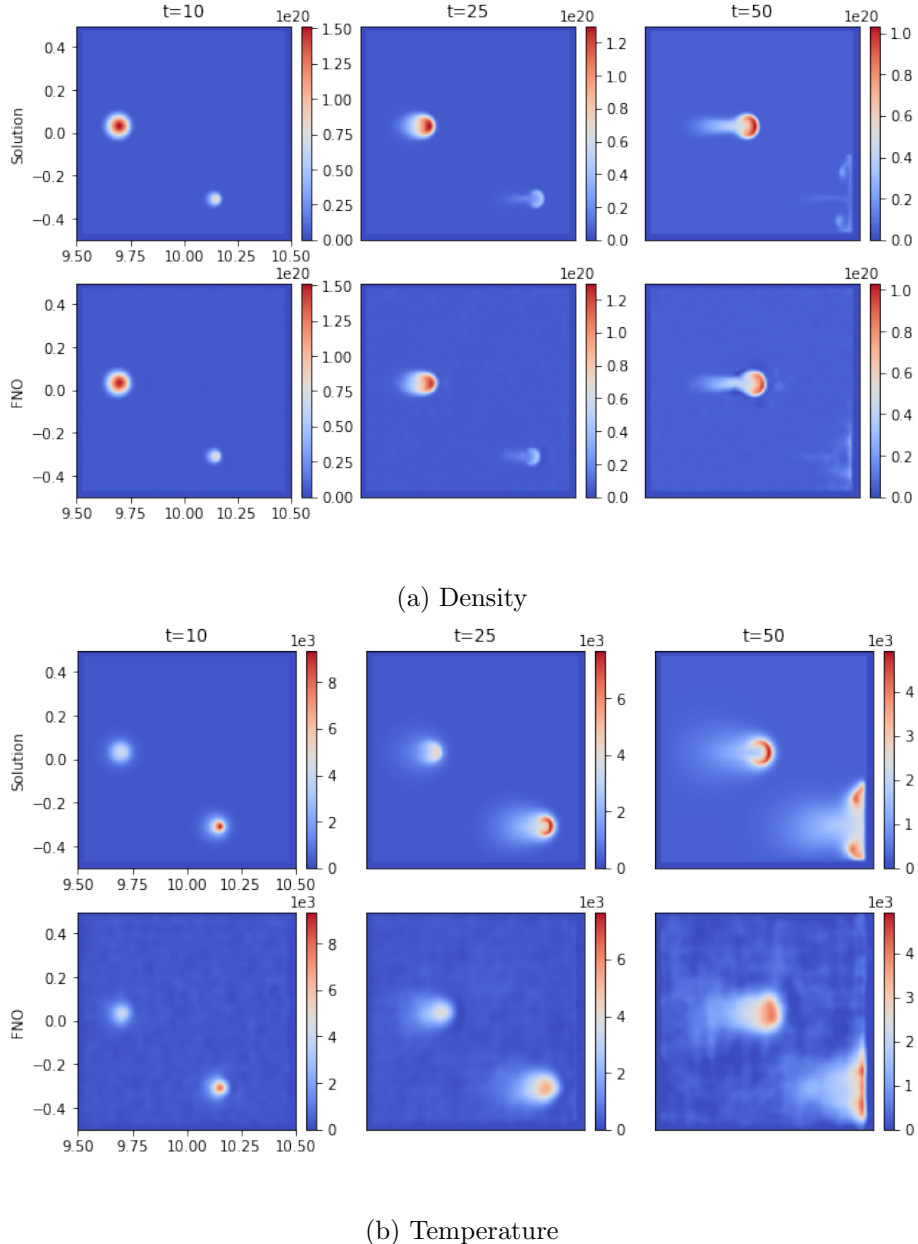


Figure 27: Multiple Blobs: Temporal evolution of (a) the density and (b) the temperature variables describing the plasma evolution as obtained using the JOREK code (top of each image) and that of the multi-variable FNO (bottom of each figure). The spatial domain is given in toroidal geometry characterised by R in the x-axis and Z in the y-axis.

Appendix F. Empirical Coverage of Foundation Physics Models

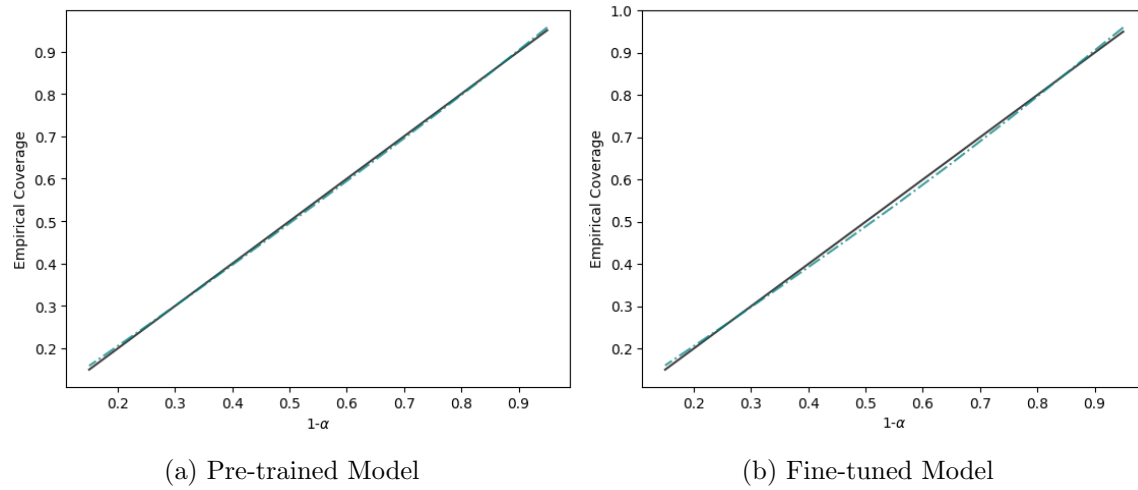


Figure 28: Empirical Coverage for Foundation Physics Models.

Appendix G. Impact of Calibration Size

Across almost all the experiments in Section 3, we use a calibration dataset of the size 1000 exchangeable simulations. The only exception is for the multi-variable FNO for MHD, for which we use 100 simulations as there was limited data available. We chose the number 1000 as the baseline size of the calibration dataset since in (Angelopoulos and Bates, 2023) they demonstrate that choosing $n_{cal} = 1000$ calibration points leads to a coverage that is typically between 0.88 and 0.92 for $\alpha = 0.1$. Since the size and nature of the calibration set is a source of finite sample variability, it requires analysis across each problem to which we deploy CP.

Ideally Equation (1) holds for a calibration dataset of any size n_{cal} . The coverage guaranteed by CP conditionally on this calibration dataset is essentially a random quantity. Thus, depending on the choice of the calibration dataset, the coverage would fluctuate around $1 - \alpha$. The distribution of the coverage as a function of the size of the calibration size is governed by a Beta distribution as given in Equation (4).

We conduct an empirical study exploring the impact the size of the calibration dataset has on providing guaranteed coverage within our experiments. We iterate over $n_{cal} = 250, 500, 750, 1000$ for the Poisson (Figure 29), Convection-Diffusion (Figure 30) and the Wave Equation (Figure 31, 32). Though the coverage obtained is from a Beta distribution governed by n_{cal} and changes with each sampling from that, our experiments are restricted to a single sample of n_{cal} data points from that distribution. The study of the impact of the calibration dataset is done across all the various nonconformity scores as well.

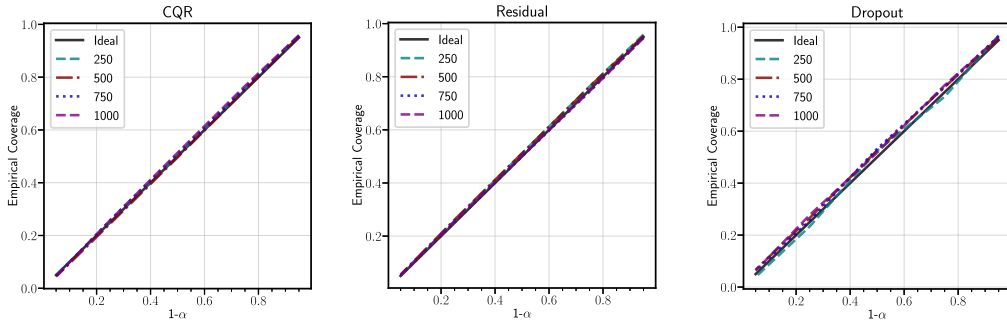


Figure 29: Impact of the size of the calibration dataset on the coverage obtained for Conformal Prediction across various nonconformity scores for the **Poisson Equation**. Irrespective of the chosen size of the calibration dataset, we obtain guaranteed coverage.

From Figure 29 to Figure 32, we explore the impact of the size of the calibration dataset on the coverage obtained for the various nonconformity scores. We notice that across our experiments, we obtain guaranteed coverage, irrespective of the chosen nonconformity score or the size of the calibration dataset (n_{cal}). Though the size of the calibration dataset has no impact on the guarantee as can be witnessed in the above figures, the tightness of the error bars is governed by the size of the calibration dataset.

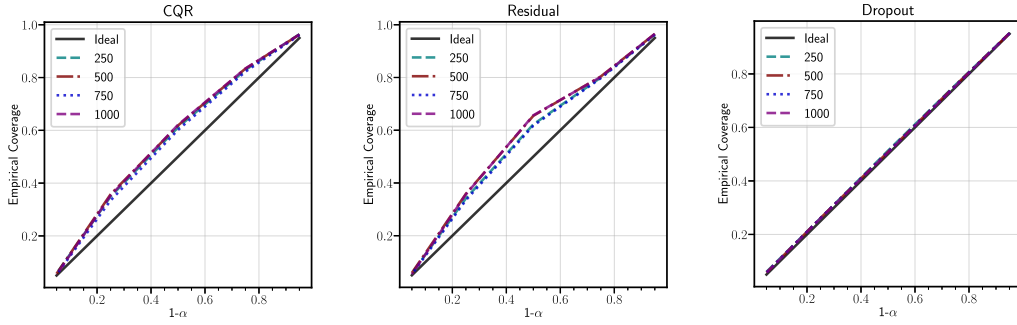


Figure 30: Impact of the size of the calibration dataset on the coverage obtained for Conformal Prediction across various nonconformity scores for the **Convection-Diffusion Equation**. Irrespective of the chosen size of the calibration dataset, we obtain guaranteed coverage, however with larger n_{cal} we obtain marginally better coverage. Irrespective of the chosen size of the calibration dataset, we obtain guaranteed coverage.

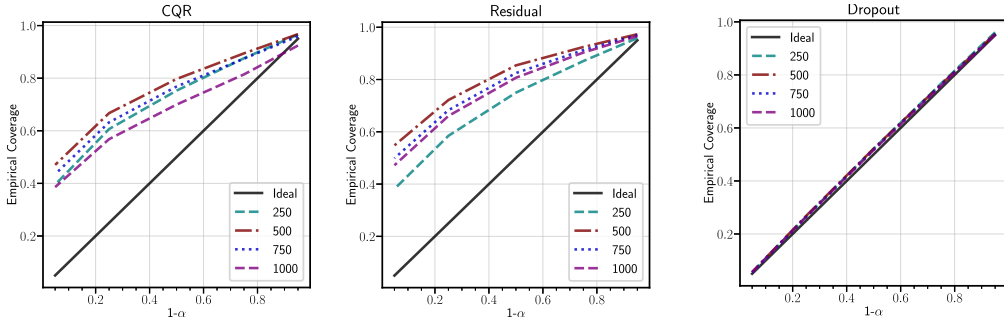


Figure 31: Impact of the size of the calibration dataset on the coverage obtained for Conformal Prediction across various nonconformity scores for the **Wave Equation modelled using U-Net**. Irrespective of the chosen size of the calibration dataset, we obtain guaranteed coverage.

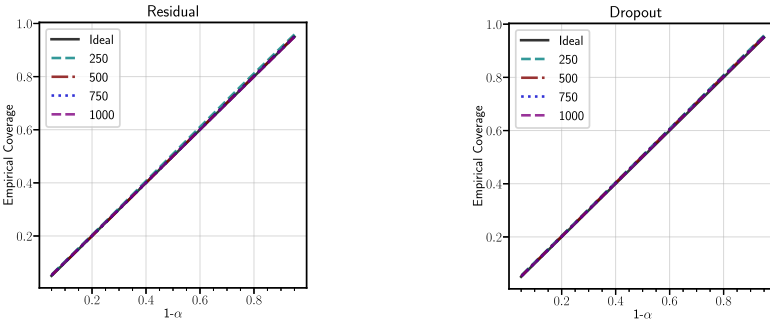


Figure 32: Impact of the size of the calibration dataset on the coverage obtained for Conformal Prediction across various nonconformity scores for the **Wave Equation modelled using FNO**. Irrespective of the chosen size of the calibration dataset, we obtain guaranteed coverage.

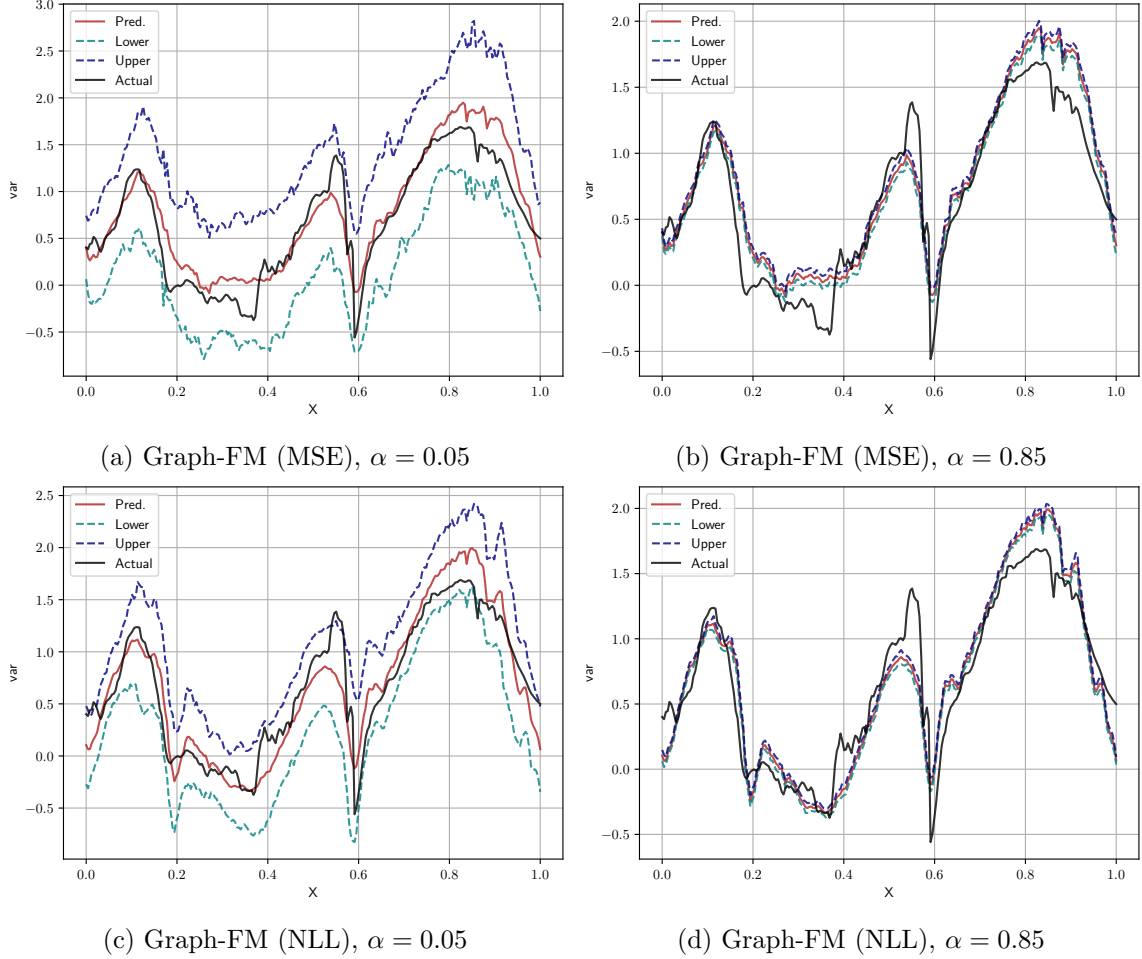


Figure 33: Slice plots across the x -axis of a temporal prediction of a single variable (u-component of wind). Figures (a) - (d) depicts the ground truth, prediction, upper and lower bars obtained through the CP framework for the Graph-FM (MSE) and Graph-FM (NLL) for 95 percent coverage ($\alpha = 0.05$) and 15 percent coverage ($\alpha = 0.85$).

Appendix H. Additional Results for Weather Forecasting Models

We here include some additional plots from the weather forecasting experiments. In Figure 33 we show slice plots along the limited area spatial domain. This further illustrates the error bars obtained at various coverage levels using the CP framework. Figure 34 shows empirical coverage for example variables in global weather forecasting.

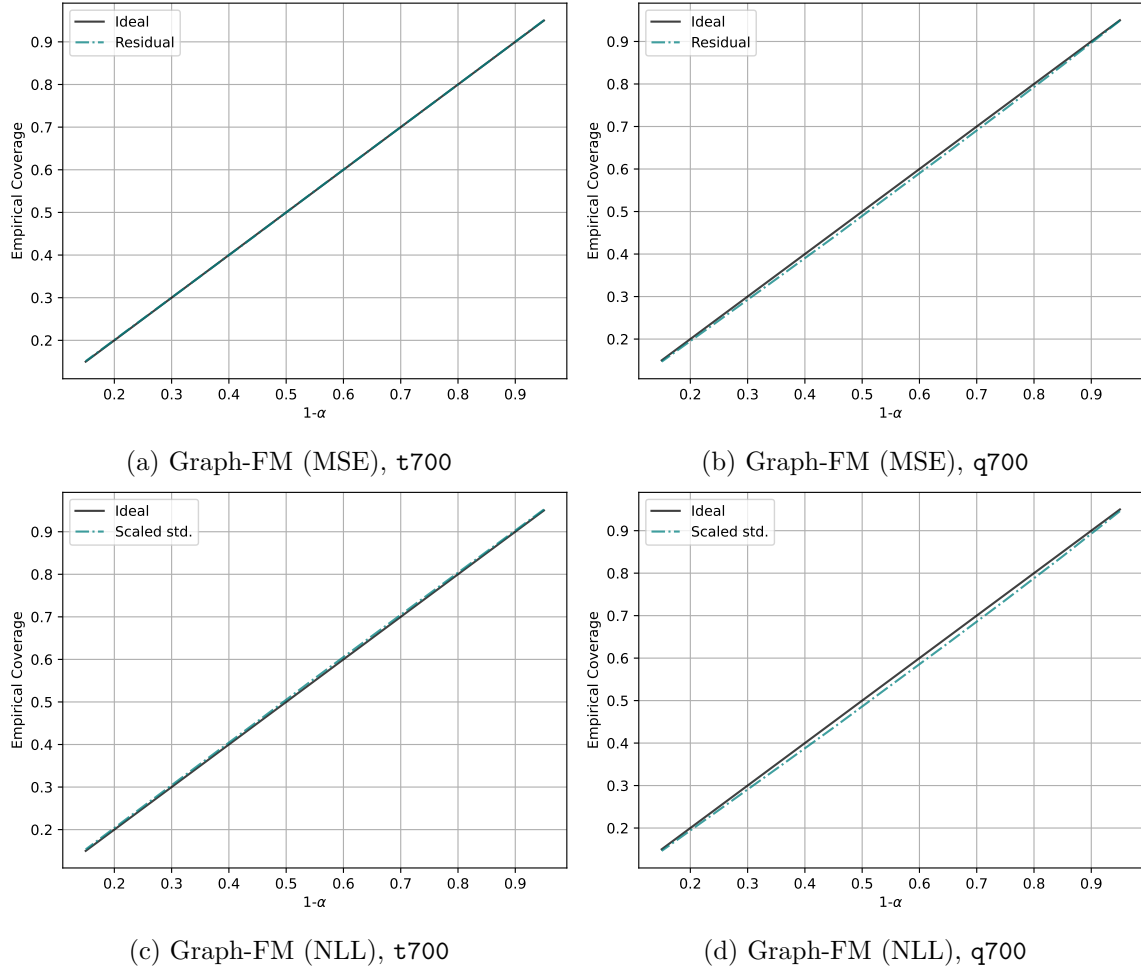


Figure 34: Empirical coverage for global weather forecasting models. We here plot the empirical coverage per variable, for temperature (t700) and geopotential (q700) at 700 hPa.

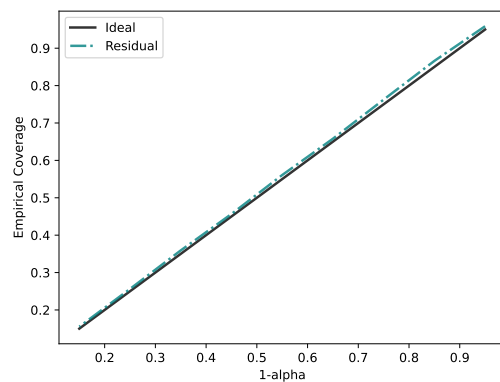


Figure 35: Empirical Coverage guaranteed by applying CP over the FNO forecasting the plasma evolution.

Appendix I. Camera Diagnostic on a Tokamak